

Finite Element Analysis of Automobile Front Axle

Abish Paudel¹

Bikash Mehta²

^{1,2}A Project Submitted in Partial Fulfillment of the Requirements for the Degree of Master of Science in Mechanical Engineering

Advisory Committee:

Dr. Soondo Kweon, Ph.D³

Dr. Fengxia Wang, Ph.D⁴

Dr. Kamran Shavezipur, Ph.D⁵

^{3, 4, 5} Graduate School Southern Illinois University Edwardsville

Publication Date: 2025/05/29

How to cite: Abish Paudel; Bikash Mehta; Dr. Soondo Kweon, Ph.D; Dr. Fengxia Wang, Ph.D; Dr. Kamran Shavezipur, Ph.D (2025). Finite Element Analysis of Automobile Front Axle. *International Journal of Innovative Science and Research Technology*, 10(5), 2215-2246.
<https://doi.org/10.38124/ijisrt/25may769>

ABSTRACT

The front axle is a critical structural component in vehicles, playing a pivotal role in supporting weight, facilitating steering, and absorbing shocks from uneven surfaces. Constructed from high-strength materials like steel or alloyed metals, its design varies based on vehicle type and performance requirements. This study specifically focuses on the front dead axle used in rear-wheel-drive vehicles, which serves as a structural support and steering mechanism without transmitting driving torque. Emphasis is placed on understanding the mechanical behavior of the front dead axle under extreme loading conditions, particularly during a frontal crash scenario with a load equivalent to 5G. The axle's structural components—such as the main beam and kingpins—are analyzed for their role in ensuring safety and stability.

In this paper, structural analysis of the front axle is conducted using ABAQUS with a crash load of 5G to the front-end of the front axle. An optimized front axle is designed and further FE (Finite Element) analysis is performed. Static FE analysis is performed on a CAD (Computer Aided Design) model and the performance in both elastic & elastoplastic cases are checked. The results indicate that an optimized design reduces the maximum stress experienced by the axle, thereby increasing the factor of safety. With a factor of safety equal to or greater than 1 under a reduced crash load of 5G, the study confirms the axle's ability to withstand severe loading scenarios. Validation of the Abaqus result is done with a MATLAB FE code, which is developed in this study and the Abaqus results are in agreement with the MATLAB FE code result. This research underscores the value of FEA in guiding design optimization, enabling safer and more efficient vehicle components through simulation-driven engineering.

ACKNOWLEDGEMENT

I would like to start by expressing my heartfelt appreciation to my parents, instructors, and friends who have unwaveringly supported me during my time at SIUE. Their constant support and love have been invaluable throughout my graduate journey.

I am deeply grateful to my advisor, Dr. Soondo Kweon, whose expertise, sincere guidance, and timely feedback have significantly contributed to the success of this work. Additionally, I want to extend my thanks to the members of my committee for their assistance, support, and encouragement.

CONTENTS

ABSTRACT.....	2216
ACKNOWLEDGEMENT.....	2217
CHAPTER ONE INTRODUCTION	2221
CHAPTER TWO LITERATURE REVIEW	2222
CHAPTER THREE METHODOLOGY	2224
➤ <i>Theory</i>	2224
• <i>Mapping</i>	2224
➤ <i>FEM Coding & Solving Procedure:</i>	2231
➤ <i>MATLAB code function structure:</i>	2232
• <i>MATLAB Function in Brief</i>	2233
➤ <i>Verification of Matlab Code</i>	2233
• <i>Verification Using One Element Model</i>	2233
➤ <i>Verification Using 8 Element Model</i>	2234
➤ <i>Verification Using 64 Element Model</i>	2235
CHAPTER FOUR MODELING AND SIMULATION.....	2237
➤ <i>Static Analysis</i>	2239
➤ <i>Boundary Conditions</i>	2240
➤ <i>Mesh</i>	2241
CHAPTER FIVE RESULT AND ANALYSIS	2242
➤ <i>Model 1</i>	2242
• <i>Elastic Analysis</i>	2242
➤ <i>Elastoplastic Analysis</i>	2242
➤ <i>Elastoplastic Analysis</i>	2243
➤ <i>Summary of the results</i>	2244
CHAPTER SIX CONCLUSION.....	2245
REFERENCES	2246

LIST OF FIGURES

Figure 1: Live (Left) & Dead Axle (Right).....	2221
Figure 2: Element Mapping	2224
Figure 3: Iso-parametric 1-D elements mappings.....	2225
Figure 4:Iso-parametric 2D elements mappings.....	2226
Figure 5:2D element mappings	2227
Figure 6:Newton Raphson solving procedure	2229
Figure 7:Matlab function structure	2232
Figure 8 One Element Model	2233
Figure 9 Reaction force vs displacement comparison for one element.....	2234
Figure 10 Meshing of 8-elements cube model	2234
Figure 11 Reaction force vs displacement comparison for 8-element model.....	2235
Figure 12 Meshing of 64-elements cube model	2235
Figure 13 Reaction Force vs Displacement Comparison For 64-Element Model.....	2236
Figure 14 Cross Section of Front Axle	2237
Figure 15 Left View of Front Axle.....	2238
Figure 16 Top View of Front Axle.....	2238
Figure 17 Model Parameters for modifications.....	2239
Figure 18 Boundary conditions at the center (A) and kingpin (B).....	2240
Figure 19 Loading conditions at the contact area	2241
Figure 20 Tetrahedral mesh on model	2241
Figure 21 Model 1: Elastic Analysis.....	2242
Figure 22 Model 1: Elastoplastic Analysis.....	2242
Figure 23 Model 2: Elastic Analysis.....	2243
Figure 24 Model 2: Elastoplastic Analysis.....	2243

LIST OF TABLES

Table 1: Model Definition.....	2239
Table 2: Mechanical Properties of Material.....	2239
Table 3:Material Composition.....	2239
Table 4: Summary of Simulation Results	2244

CHAPTER ONE INTRODUCTION

The front axle plays a crucial role in the assembly of various wheeled machines, especially in cars, trucks, and other vehicles. It acts as a crucial component for bearing weight and transferring motion, essential for the steering, suspension, and overall stability of the vehicle. The front axle not only bears the vehicle's weight but also enables seamless and effective movement by linking the front wheels for precise steering and shock absorption on rough surfaces.

It is usually made of strong substances like steel or alloyed metals and is built to withstand intense stress and weight. Its composition changes according to the vehicle's type and intended use. Heavy-duty trucks need a front axle that can bear heavy loads and fit larger steering systems, while passenger cars need axles designed for comfort, performance, and easy handling but which are also lightweight. The axle is made up of many important parts like the main beam, stub axles, kingpins, ball joints, bearings, bushes, and shock absorbers. Every component plays a role in making the axle work efficiently, by offering points for turning and minimizing friction for easy wheel movement.

The front axle plays several important roles that are necessary for the performance and safety of the vehicle. It bears the load of the front part of the car, which consists of the engine and occupants. It allows for precise control of steering by enabling the wheels to move at angles with the help of a steering gear box. Additionally, it serves an important function in dampening shocks and vibrations from bumpy roads, due to its connection with the suspension system guaranteeing a smoother journey.

There are two main types of front axles classified according to their function. The front wheels of vehicles with all-wheel-drive and four-wheel-drive systems have a live front axle, which means they are also responsible for driving the vehicle. This category facilitates the transfer of torque while aiding in moving dynamically. On the flip side, the dead front axle acts as a supporting framework and steering center in rear-wheel-drive cars.

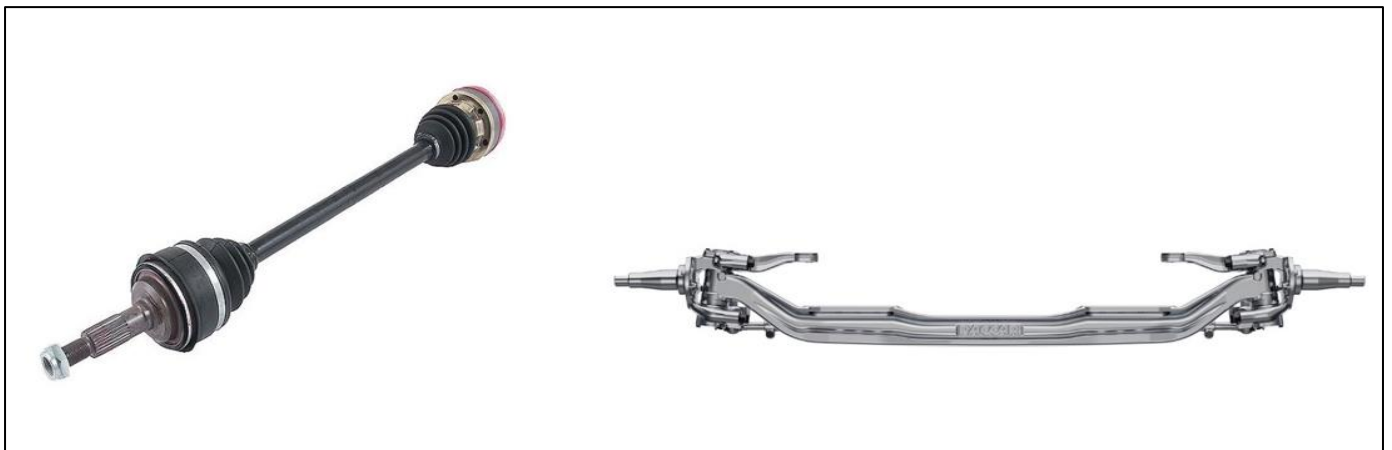


Fig 1 Live (Left) & Dead Axle (Right)

This study focuses on the Finite Element Analysis (FEA) of a front dead axle under a frontal crash load of 5G. Due to the absence of an analytical solution for structures with complex 3D geometries, a numerical approach using Finite Element Analysis is employed.

The primary objective is to gain a comprehensive understanding of the behavior of the front dead axle when subjected to the specified crash load, enabling insights into its performance and optimization.

CHAPTER TWO LITERATURE REVIEW

Min Zhang et al. (2016) analyzed the strength and fatigue life of a front axle using the fatigue tool in ANSYS Workbench. By modeling the front beam made of 50 steel under various working conditions, including full load, braking, and cornering, the study identifies that the critical area is located at the variable cross-section beneath the plate spring. To optimize the strength of the beam, the web is stretched in the design, ensuring that the lower surface experiences no bending.

Shwetank Avikal et al. (2020) researched the design and fatigue analysis of the front axle beam of a heavy-duty truck using ANSYS Workbench. The study aims to optimize the fatigue life of the axle beam by comparing five different materials: 50 steel, AISI 1045, AISI 4130, AISI 4140, and AISI 4150. Various FEM analysis results are compared, leading to the recommendation of suitable material. The researchers find that minimum deformation occurs with 50 steel and propose its use in cases where space below the axle beam is limited. Additionally, the study concludes that AISI 4150 offers the longest fatigue life for axle beams and is the most suitable material when high fatigue life is desired for heavy-duty vehicles.

Topaç et al. (2009) conducted a finite element analysis using ANSYS workbench to predict the fatigue life of a rear axle housing prototype under dynamic vertical loads. The researchers identify the banjo transition area of the carrier mounting side of the lower shell as the critical regions where fatigue failure occurs due to the stress concentration during testing. Fatigue cracks initiate in these areas due to cyclic tensile stress, which leads to premature failure before reaching the expected load cycles. To improve the durability of the axle, the authors propose redesigning the transition geometry and increasing the thickness of the reinforcement ring. These modifications help reduce stress concentration and extend the fatigue life of the axle.

Aghav et al. (2016) conducted stress and fatigue analysis of the front axle beam of a heavy-duty truck using ANSYS Ncode Design Life software. The researchers identify the spring pad as the critical region where maximum stress occurs under vertical loading and the goose neck as the critical region under vertical and braking loading. Fatigue cracks initiate in these regions due to fluctuating loads caused by road surface irregularities and braking forces. The analysis demonstrates that the front axle beam has a fatigue life exceeding 2×10^5 cycles for vertical loading and 4×10^3 cycles for vertical and braking loads, which confirms that the design is safe under both conditions.

Zheng B et al. (2022) conducted a comprehensive study on the topology and multiobjective optimization of the drive axle housing for a rear axle drive truck. They built on existing research by combining static, dynamic, and fatigue analyses to evaluate the performance of the drive axle housing under four critical working conditions: maximum vertical force, traction, lateral force, and braking. Their analysis reveals that the maximum vertical force condition results in the highest equivalent stress at the step of the half-shaft casing, a key area prone to damage in real-world applications. To mitigate this, the authors implement a topology optimization approach, reducing the axle housing's mass by 17.4%. This significantly improves other critical parameters, including a 21.05% reduction in equivalent stress and a 72.28% increase in minimum fatigue life, enhancing both durability and overall performance.

Deshmukh et al. (2018) focused on the topology optimization of the rear axle in heavy vehicles, aiming to improve performance while reducing weight. Their study uses static analysis and topology optimization techniques to identify critical areas under real loading conditions. By refining the geometry and material distribution, including adding a truss structure, they successfully reduce the axle's mass by 11.07%. This optimization leads to improved stress distribution and a 23.85% enhancement in weight-carrying capacity.

Duble et al (2020) conducted a study on the design and finite element analysis (FEA) of the differential cover for the rear drive axle of a light commercial vehicle (LCV). They addressed common issues such as premature failure, bolt loosening, and oil leakage by performing multiple FEA iterations with adjustments to wall thickness and hole sizes. Their optimized design, using the SAPH440 material, improved the fatigue life of the differential cover beyond the target cycles. The study demonstrates the effectiveness of FEA enhancing the structural integrity of the differential cover, achieving significant improvements in fatigue resistance, and eliminating oil leakage from the cover mating surface.

Sainadh et al. (2018) researched the importance of analyzing the front axle in electric vehicles under severe load conditions. The kingpin stub axle assembly, a critical component, efficiently manages vertical loads and cornering stresses. Through the use of finite element analysis (FEA), the axle is optimized for material selection, which enhances its strength while minimizing weight. The findings demonstrate that the AISI 304 steel provides an optimal balance of performance and durability, making it a suitable choice for the front axle design in electric vehicles.

León et al. (2000) conducted a study on reducing the weight of a truck's frontal axle beam by combining finite element analysis (FEA) with experimental validation. The objective is to decrease material and manufacturing costs while keeping stress levels within acceptable limits. Through iterative parametric improvements, the researchers achieved a 6.8% weight reduction without exceeding the permissible stress values. The integration of CAD, FEA, and experimental methods, particularly MSC.Patran and MSC.Nastran software, allowed for rapid design modifications and increased product reliability.

Dhande et al. (2014) researched and analyzed the front axle beam of a heavy commercial vehicle, providing a comparison between two materials. They performed FEM analysis using ANSYS and found that maximum deflection and stress distribution are lower for the SAE 1020 material than for a ductile cast iron. The researchers conclude that an axle beam made from SAE 1020 can perform well even under high-stress conditions.

Topaç et al. (2012) conducted a finite element analysis to predict the fatigue life of a heavy vehicle steel wheel subjected to radial loads. The researchers identified the air ventilation holes as the critical region where fatigue failure occurs due to stress concentration during testing. The fatigue cracks initiate in these regions due to circumferential stress during wheel rotation. To improve the wheel's durability, the authors propose a design enhancement involving an increase in the local thickness and the cross-sectional radius around the ventilation holes, which reduces stress concentration. By applying these modifications, they extend the fatigue life of the wheel, demonstrating that their computational methods can reliably predict failure locations and improve component durability.

CHAPTER THREE METHODOLOGY

➤ *Theory*

• *Mapping*

The primary objective of element mapping is to enable the construction of geometrically complex elements with curved boundaries while preserving essential properties and relationships between the parent (local) and global coordinate systems. This process establishes a correspondence between the parent coordinates (denoted as ξ and η) and the global coordinates (x and y). Two distinct mapping frameworks are employed for this purpose:

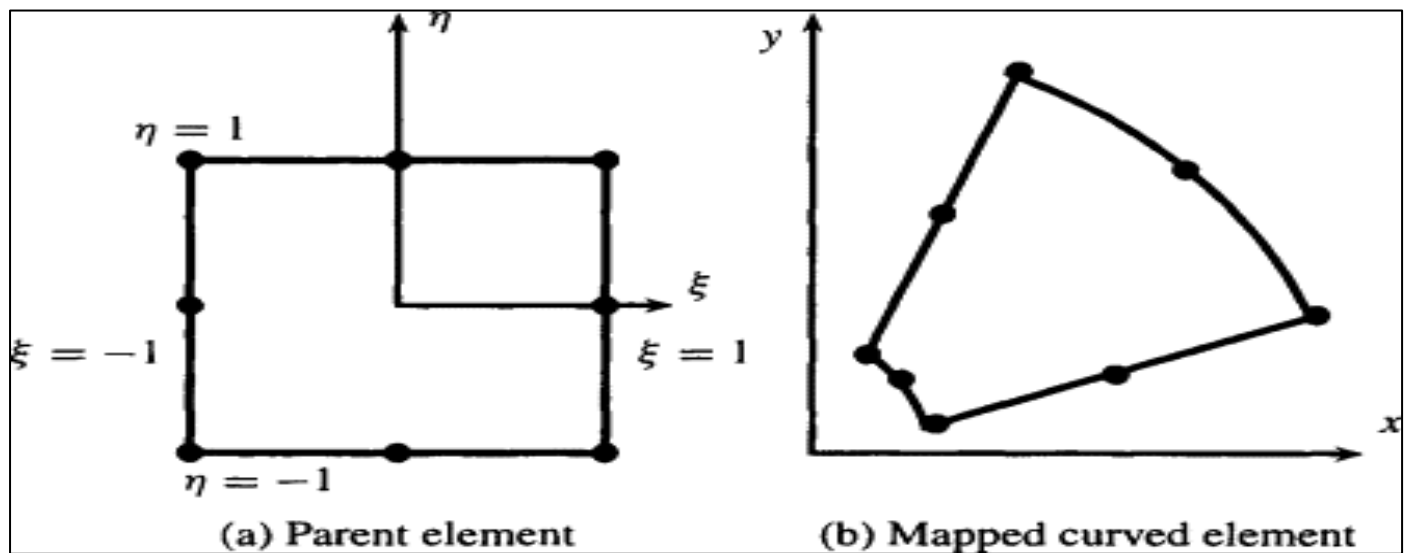


Fig 2 Element Mapping

- The first one is for the unknown solution field (i.e. Displacement, Temperature, etc.)

$$T(x, y) \text{ or } U(x, y) \approx \tilde{T}(x, y) = \langle N \rangle \{d\} \dots\dots (1)$$

In the above equation, T refers to the temperature field and U refers to the displacement field.

Where,

$\langle d \rangle = \langle T_1, T_2, T_3, T_4, \dots, T_M \rangle =$ Vector with unknown nodal values

$\{d\} = \langle d \rangle^T$, $\{d\}$: Column vector, $\langle d \rangle = \{d\}^T$: Row vector

- The second one is for the coordinates

$$\begin{Bmatrix} x \\ y \end{Bmatrix} = [\tilde{N}] \{c\} \dots\dots (2)$$

Where,

$\langle c \rangle = \langle x_1, y_1, x_2, y_2, x_3, y_3, \dots, x_M, y_M \rangle =$ Vector with nodal coordinates.

➤ *Shape Functions and Element Classification*

In mapped elements, the behavior is governed by two sets of shape functions: N (for approximating the solution field) and \tilde{N} (for geometric mapping). The choice of shape functions determines the element type, categorized as follows:

- An iso-parametric (or ‘same parameter’) element is one for which $N \equiv \tilde{N}$
- A sub-parametric element is such that the degree of $N >$ degree of \tilde{N}
- A super-parametric element is such that the degree of $N <$ degree of \tilde{N}

Since the mapping complicates the formulation of residual in its equation, it needs numerical integration.

• *Iso-Parametric 1-D Element:*

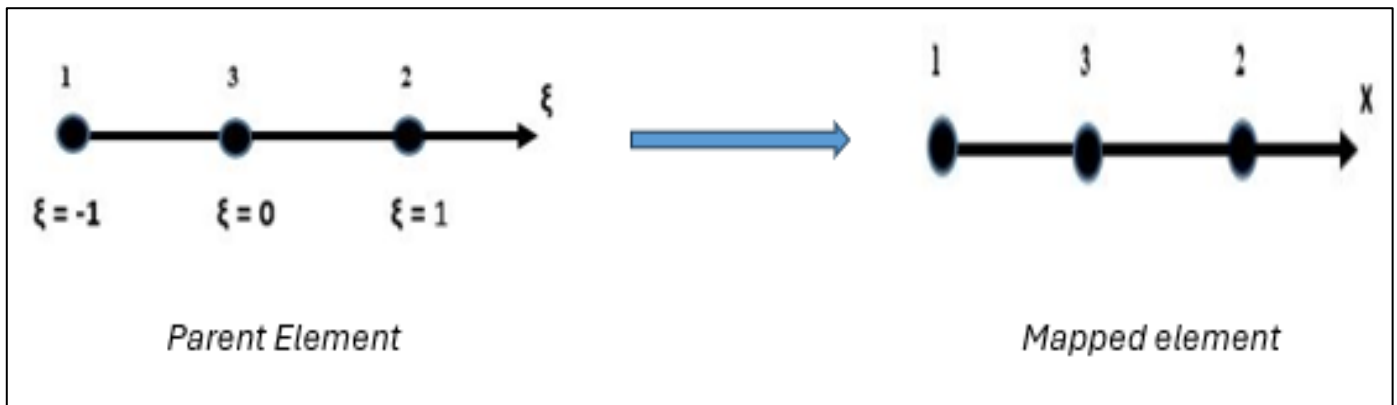


Fig 3 Iso-Parametric 1-D Elements Mappings

Shape functions for a one-dimensional iso-parametric elements:

$$N_1(\xi) = \frac{-\xi(1 - \xi)}{2}$$

$$N_2(\xi) = \frac{\xi(1 + \xi)}{2}$$

$$N_3(\xi) = 1 - \xi^2$$

• *Geometric Mapping:*

$$X(\xi) = \sum_{i=1}^3 x_i N_i(\xi) = x_1 N_1(\xi) + x_2 N_2(\xi) + x_3 N_3(\xi) \dots \dots \dots (3)$$

i.e.

$$\xi = -1, \text{ gets mapped onto, } x = x_1$$

$$\xi = 0, \text{ gets mapped onto, } x = x_3$$

$$\xi = 1, \text{ gets mapped onto, } x = x_2$$

$$\xi = \frac{1}{2}, \text{ gets mapped onto, } x = -\frac{1}{8}x_1 + \frac{3}{8}x_2 + \frac{6}{8}x_3$$

$$\text{Residual equation} = - \int \underline{\sigma} : \underline{\varepsilon} \, dV + \int_{S_T} \underline{T} \cdot \underline{u} \, ds + \int_V \underline{b} \cdot \underline{u} \, dV \longrightarrow [\text{For 1-D \& Ignore } \underline{b} \text{ (i.e., } \underline{b} = 0 \text{)}]$$

$$R = - \int \underline{\sigma} : \underline{\varepsilon} \, dx + \sum \underline{T}^{sp} \cdot \underline{u} \dots \dots \dots (4)$$

$$\underline{\varepsilon} = \frac{du}{dx} = \langle B \rangle \{d\} = \langle B \rangle \begin{Bmatrix} u_1 \\ u_2 \\ u_3 \end{Bmatrix},$$

Where,

$$\langle B \rangle = \frac{d}{dx} \langle N \rangle$$

$$\langle N \rangle = \langle N(\xi) \rangle = \langle N_1, N_2, N_3 \rangle = \left\langle \frac{-\xi(1 - \xi)}{2}, \frac{\xi(1 + \xi)}{2}, 1 - \xi^2 \right\rangle$$

And

$$\langle B \rangle = \frac{d}{dx} \langle N \rangle = \frac{d}{d\xi} \langle N \rangle \frac{d\xi}{dx} ; J = \frac{dx}{d\xi} = \frac{d}{d\xi} x$$

$$x(\xi) = \sum_{i=1}^3 x_i N_i\{\xi\}$$

$$J(\xi) = \frac{dx}{d\xi} = \sum_{i=1}^3 x_i \frac{dN_i\{\xi\}}{d\xi} \quad \text{with} \quad \langle \frac{dN}{dx} \rangle = \langle \frac{-1+2\xi}{2}, \frac{1+2\xi}{2}, -2\xi \rangle$$

Therefore, $\langle B \rangle = \frac{d}{dx} \langle N \rangle = \frac{1}{J(\xi)} \langle \frac{dN}{d\xi} \rangle$

• Iso-parametric 2-D elements:

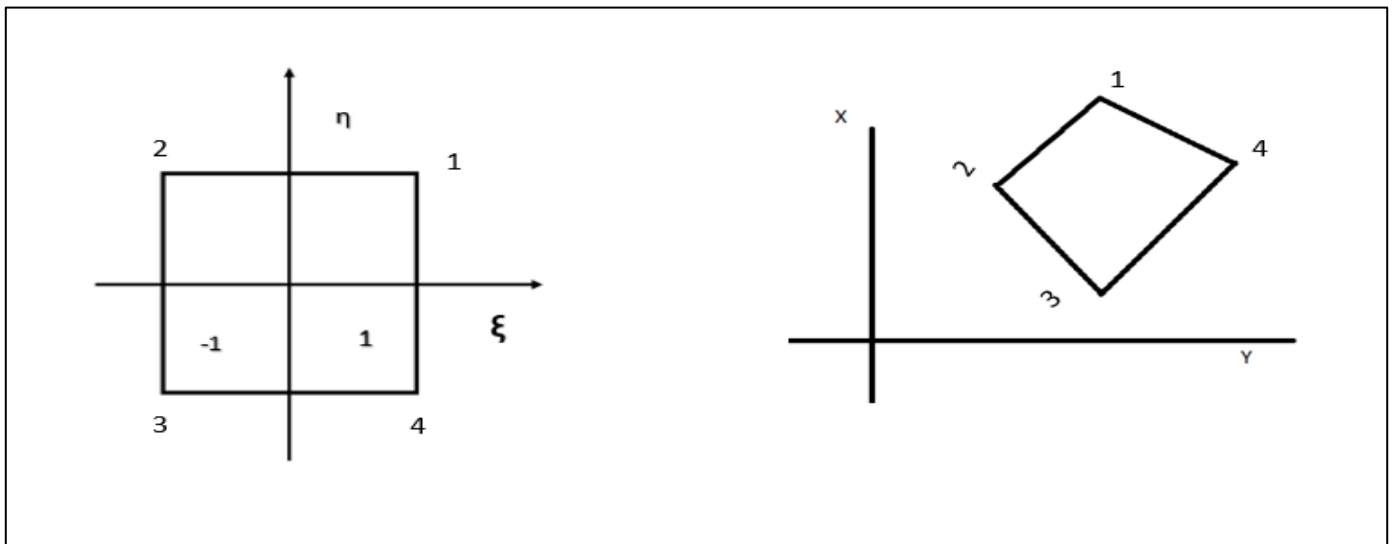


Fig 4 Iso-Parametric 2D Elements Mappings

Shape functions:

$$N_1(\xi, \eta) = \frac{(1+\xi)(1+\eta)}{4}$$

$$N_2(\xi, \eta) = \frac{(1-\xi)(1+\eta)}{4}$$

$$N_3(\xi, \eta) = \frac{(1-\xi)(1-\eta)}{4}$$

$$N_4(\xi, \eta) = \frac{(1+\xi)(1-\eta)}{4}$$

Geometric mapping:

$$X(\xi, \eta) = \sum_{i=1}^4 x_i N_i\{\xi, \eta\}$$

$$Y(\xi, \eta) = \sum_{i=1}^4 y_i N_i\{\xi, \eta\}$$

$$[B] = \begin{bmatrix} \frac{\partial N_1}{\partial x} & \frac{\partial N_2}{\partial x} & \frac{\partial N_3}{\partial x} & \frac{\partial N_4}{\partial x} \\ \frac{\partial N_1}{\partial y} & \frac{\partial N_2}{\partial y} & \frac{\partial N_3}{\partial y} & \frac{\partial N_4}{\partial y} \end{bmatrix} \dots \dots \dots (5)$$

$$\langle N \rangle = \langle N_1, N_2, N_3, N_4 \rangle$$

When N_i is already written in terms of ξ, η .

For any function ϕ , chain rule can be used as following:

$$\begin{Bmatrix} \phi, \xi \\ \phi, \eta \end{Bmatrix} = \begin{bmatrix} \frac{\partial x}{\partial \xi} & \frac{\partial y}{\partial \xi} \\ \frac{\partial x}{\partial \eta} & \frac{\partial y}{\partial \eta} \end{bmatrix} \begin{Bmatrix} \phi, x \\ \phi, y \end{Bmatrix} \dots \dots \dots (6)$$

Inverting,

$$\begin{Bmatrix} \varphi, x \\ \varphi, y \end{Bmatrix} = \begin{bmatrix} \frac{\partial \xi}{\partial x} & \frac{\partial \eta}{\partial x} \\ \frac{\partial \xi}{\partial y} & \frac{\partial \eta}{\partial y} \end{bmatrix} \begin{Bmatrix} \varphi, \xi \\ \varphi, \eta \end{Bmatrix} \dots\dots\dots (7)$$

For $\varphi = N_i$,

$$\begin{Bmatrix} \frac{\partial N_i}{\partial x} \\ \frac{\partial N_i}{\partial y} \end{Bmatrix} = [J(\xi, \eta)]^{-1} \begin{Bmatrix} \frac{\partial N_i}{\partial \xi} \\ \frac{\partial N_i}{\partial \eta} \end{Bmatrix} \dots\dots\dots (8)$$

$$\text{Residual} = - \int \underline{\sigma} : \underline{\varepsilon} : dA * \text{thickness} + \int_{ST} \underline{T} \cdot \underline{u} \, ds + \int_v \underline{b} \cdot \underline{u} \, dA * \text{thickness}$$

$$dA = \sum dA^e \quad \text{where, } dA^e \text{ is for each element}$$

$$dA^e = dx \, dy = \det [J] \, d\xi \, d\eta = \left(\frac{\partial x}{\partial \xi} \frac{\partial y}{\partial \eta} - \frac{\partial x}{\partial \eta} \frac{\partial y}{\partial \xi} \right) d\xi \, d\eta$$

$$dS = \sum ds^e \text{ where, } ds^e \text{ is for each element.}$$

$$dS^e = \text{thickness} * dS^{e'}$$

If the side is along $\eta = 1$ or $\eta = -1$

$$dS^{e'} = \sqrt{\left(\frac{\partial x}{\partial \xi}\right)^2 + \left(\frac{\partial y}{\partial \xi}\right)^2} d\xi$$

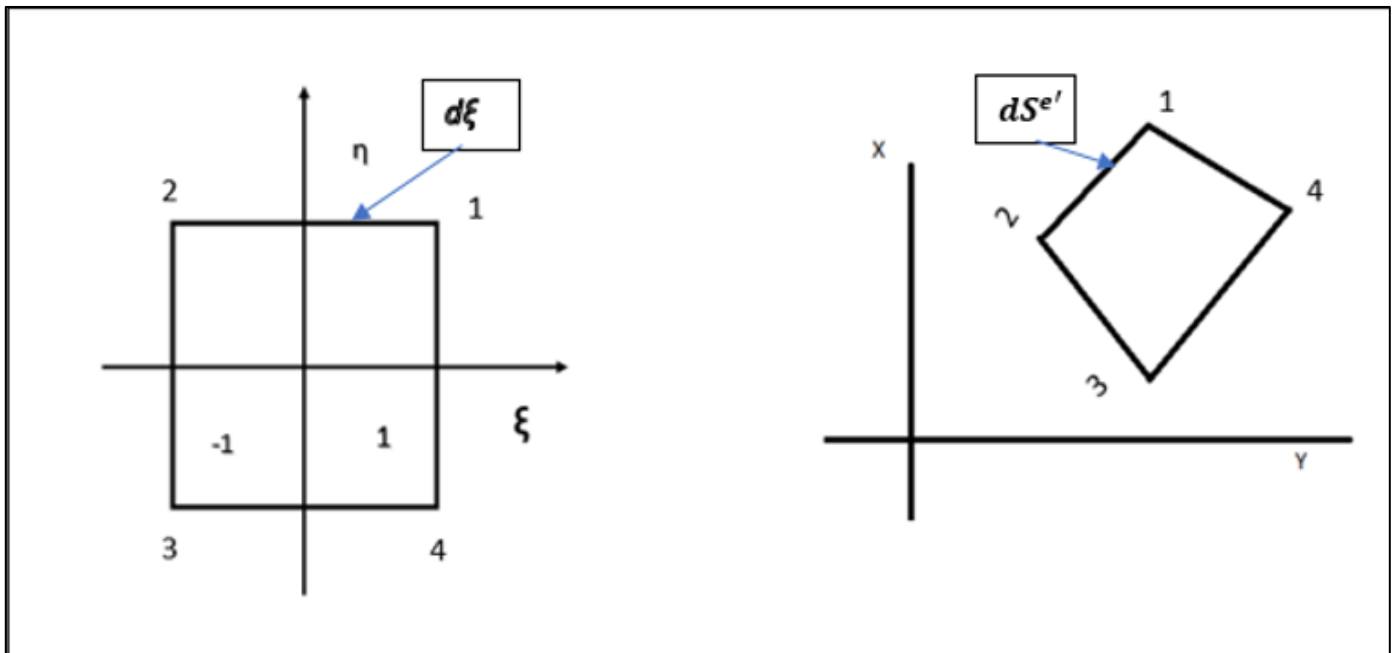


Fig 5 2D Element Mappings

If the side is along $\xi = 1$ or $\xi = -1$,

$$dS^{e'} = \sqrt{dx^2 + dy^2} = \sqrt{\left(\frac{\partial x}{\partial \eta}\right)^2 + \left(\frac{\partial y}{\partial \eta}\right)^2} d\eta \dots\dots\dots (9)$$

In 2-D,

$$\underline{\epsilon} = \frac{\partial y}{\partial x} = \frac{\partial \langle N \rangle}{\partial x} \{d\} = \begin{bmatrix} \frac{\partial N_1}{\partial x} & \frac{\partial N_2}{\partial x} & \frac{\partial N_3}{\partial x} & \frac{\partial N_4}{\partial x} \\ \frac{\partial N_1}{\partial y} & \frac{\partial N_2}{\partial y} & \frac{\partial N_3}{\partial y} & \frac{\partial N_4}{\partial y} \end{bmatrix} \begin{bmatrix} U_1 & V_1 \\ U_2 & V_2 \\ U_3 & V_3 \\ U_4 & V_4 \end{bmatrix} \dots\dots\dots(10)$$

$$\underline{u} = \langle N \rangle \{d\} = [N_1, N_2, N_3, N_4] \begin{bmatrix} U_1 & V_1 \\ U_2 & V_2 \\ U_3 & V_3 \\ U_4 & V_4 \end{bmatrix} \dots\dots\dots(11)$$

$$\text{Residual} = \sum_{\text{Residual element}}$$

Henceforth, body force is ignored for the practicality.

$$\text{Residual}^{\text{element}} = - \int \underline{\sigma} : \underline{\epsilon} \, dV + \int_{S_T} \underline{T} \cdot \underline{u} \, dS$$

$$\underline{\sigma} = 3 \times 3, \underline{\epsilon} = 3 \times 3, \underline{T} = 3 \times 1, = 3 \times 1 \text{ (For 3D element)}$$

$$\sigma = \sigma(u).$$

Nonlinear response is assumed since plasticity is in general nonlinear.

Principle of virtual work should be true for all \underline{u} (all variational displacement fields).

$$\underline{u} = \langle N \rangle \{d\}$$

\underline{u} is dependent upon the number of degrees of freedom, i.e., the number of unknowns of the boundary value problem.

$$\delta R = - \int \underline{\sigma} : \underline{\epsilon} \, dV + \int_{S_T} \underline{T} \cdot \underline{u} \, dS = 0 \text{ for } \forall \delta \underline{u} \text{ i.e. } \forall \{d\} \dots\dots\dots(12)$$

This yields a system of equations equal in number to the total degrees of freedom (NDOF). With NDOF unknowns and NDOF equations, the system is well-posed and solvable.

$$\frac{\partial R}{\partial d_i} = [- \int \underline{\sigma} : [B]_i \, dV + \int_{S_T} \underline{T} \cdot \langle N_i \rangle \, dS] = 0 \dots\dots\dots(13)$$

where, $[B]_i = \frac{\partial N_i}{\partial x}$ or $\frac{\partial N_i}{\partial y}$ or $\frac{\partial N_i}{\partial z}$ (depending on i-th D.O.F.)

$$r_i \cong \frac{\partial R}{\partial d_i} = - \int \underline{\sigma} : [B]_i + \int_{S_T} \underline{T} \cdot \langle N_i \rangle \, dS = 0, (i = 1, 2, \dots, \text{NDOF})$$

$\underline{\sigma}$ is nonlinear function of d_i . Thus, the Newton-Raphson is employed to obtain the unknown d_i .

$$r_i = - \int \underline{\sigma}(d_i) : [B]_i \, dV + \int_{S_T} \underline{T} \cdot \langle N_i \rangle \, dS = 0 \dots\dots\dots(14)$$

B.V.P solving procedure.

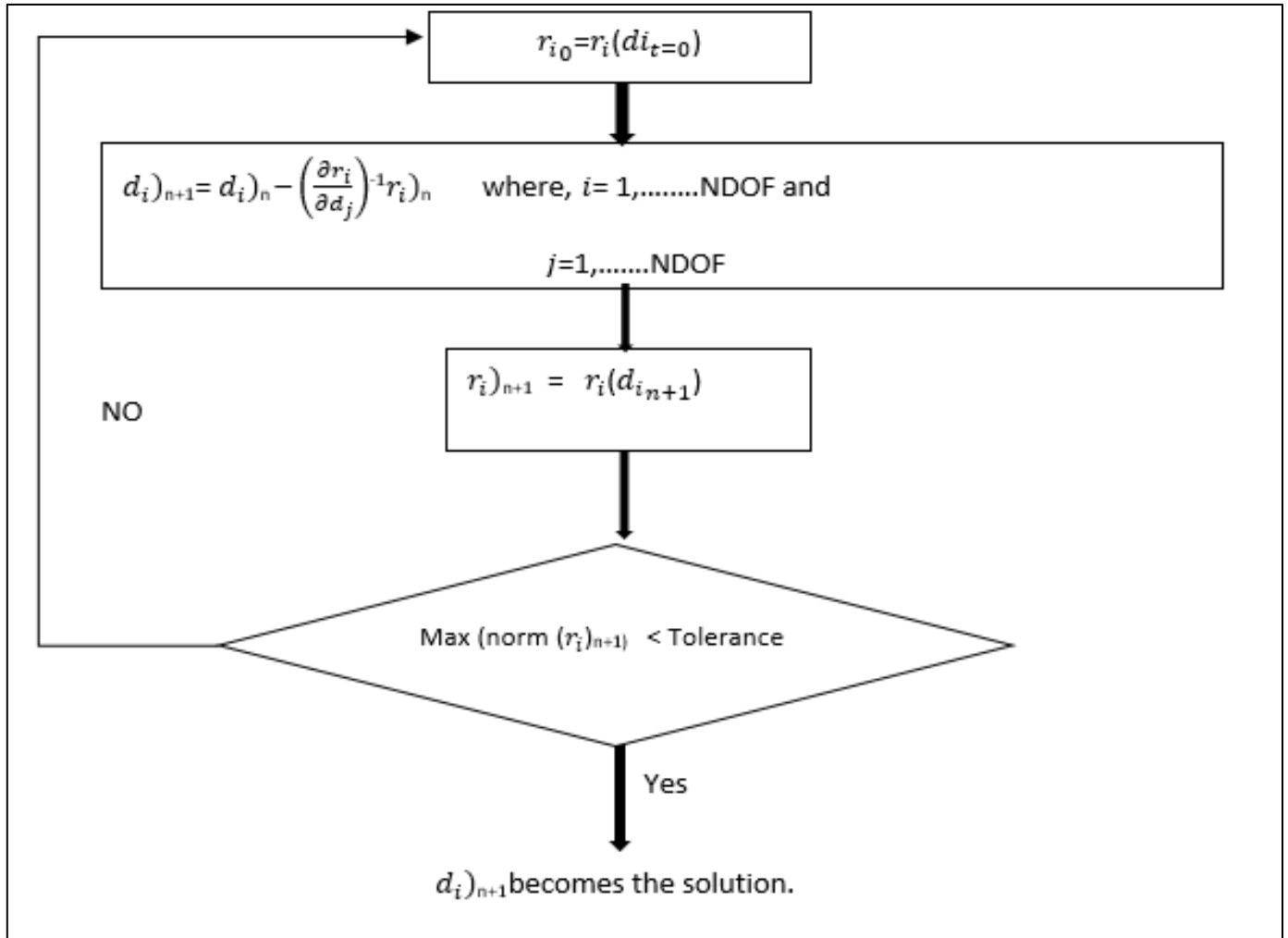


Fig 6 Newton Raphson solving procedure

After defining the differential equations and boundary conditions, the residual equation is discretized and solved using the Newton-Raphson method (Figure 6). This involves computing the Jacobian and updating the residual iteratively until its norm falls below a set tolerance, indicating convergence.

$$\frac{\partial r_i}{\partial d_j} = - \int \frac{\partial \sigma}{\partial d_j} : [B]_i \, dV \dots\dots\dots (15)$$

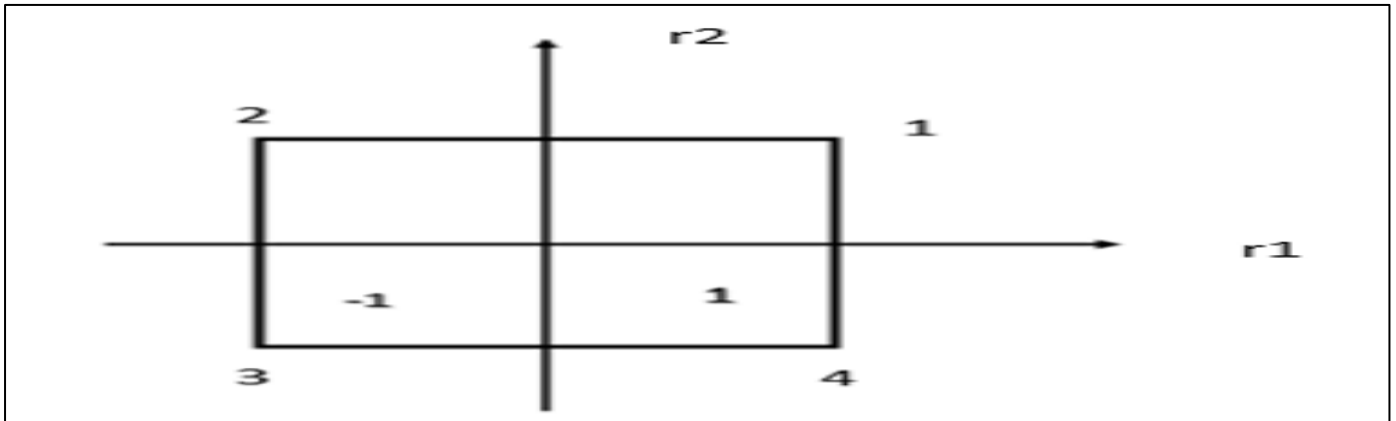
The residual is differentiated with respect to the nodal displacement, which is the main variable.

$$\frac{\partial \sigma}{\partial d_j} = \frac{\partial \sigma}{\partial \epsilon} : \frac{\partial \epsilon}{\partial d_j} \dots\dots\dots (16)$$

Using the chain rule, the differentiation is split into the stress-strain and strain-displacement relations, leading to the form shown in Equation (16).

$$\frac{\partial r_i}{\partial d_j} = - \int [B]_j : \frac{\partial \sigma}{\partial \epsilon} : [B]_i \, dV \dots\dots\dots (16)$$

$$N(\underline{r}) = \begin{bmatrix} 1/4 & (1 + r_1) & (1 + r_2) \\ 1/4 & (1 - r_1) & (1 + r_2) \\ 1/4 & (1 - r_1) & (1 - r_2) \\ 1/4 & (1 + r_1) & (1 - r_2) \end{bmatrix} \dots\dots\dots (17)$$



The equation and figure illustrate the shape functions for a four-node bilinear quadrilateral element, used to interpolate field variables (e.g., displacements) from nodal values within the element.

$$\mathcal{X} = \begin{bmatrix} x^1 & x^2 & x^3 & x^4 \\ y^1 & y^2 & y^3 & y^4 \end{bmatrix} \dots\dots\dots (18)$$

The nodal coordinates in Eq. (18) define the element geometry and are used for interpolation and numerical integration within the element's domain.

$$f(r) = x = X N(r)$$

The above equation describes the transformation between the local element coordinate and the global physical coordinate.

$$J(r) = Df(r) = X DN(r)$$

The Jacobian matrix is crucial for numerical integration, transforming derivatives between local and global coordinates, and ensuring accurate mapping in finite element analysis.

$$\mathbb{N} N(r) = \begin{bmatrix} 1/4(1 + r_2) & 1/4(1 + r_1) \\ -1/4(1 + r_2) & 1/4(1 - r_1) \\ -1/4(1 - r_2) & -1/4(1 - r_1) \\ 1/4(1 - r_2) & -1/4(1 - r_1) \end{bmatrix}$$

This vector enables coordinate interpolation within the element and is used to compute the Jacobian and other key quantities in finite element analysis.

$$\text{Displacement matrix, } U = \begin{bmatrix} U^1 & U^2 & U^3 & U^4 \\ V^1 & V^2 & V^3 & V^4 \end{bmatrix}$$

This vector represents the displacements at each node.

$$\hat{u}(r) = U N(r)$$

The displacement vector is expressed in local coordinates as shown above, and its gradient is derived as follows.

$$\nabla \hat{u}(r) = U D N(r)$$

$$\nabla \hat{u}(f(r)) = \nabla \hat{u}(r) J^{-1}(r)$$

$$= U \mathbb{N}(r) J^{-1}(r)$$

$$= I U B(r), \text{ Where } B(r) = \mathbb{N}(r) J^{-1}(r) \text{ and } I = \begin{bmatrix} 1 & 0 \\ 0 & 1 \end{bmatrix} = \text{Identity Matrix}$$

The notation illustrates how the gradient of \hat{u} with respect to local coordinates r is computed. Using \hat{u} , $N(r)$, and $J^{-1}(r)$ ensures accurate calculation of physical quantities like displacements across elements.

$$\text{vec } \nabla \underline{u} = (\mathbf{B}^T \odot \mathbf{I}) \text{vec}(\mathbf{U})$$

describes how the gradient of \underline{u} is vectorized using \mathbf{B}^T and \mathbf{I} applied to the vector \mathbf{U} .

$$= \mathbf{G}(\mathbf{r}) \text{vec}(\mathbf{U}),$$

Where

$$\mathbf{G}(\mathbf{r}) = (\mathbf{B}^T \odot \mathbf{I}), \text{vec} = (\mathbf{A}\mathbf{X}\mathbf{B}) = (\mathbf{B}^T \odot \mathbf{A}) \text{vec}(\mathbf{X})$$

$$\hat{u}(\mathbf{r}) = \mathbf{I}\mathbf{U}\mathbf{N}(\mathbf{r})$$

Represents the interpolation of \hat{u} at \mathbf{r} using the identity matrix \mathbf{I} , \mathbf{U} , and $\mathbf{N}(\mathbf{r})$

$$\text{vec}(\hat{u}(\mathbf{r})) = \mathbf{N}^T(\mathbf{r}) \odot \mathbf{I} \text{vec}(\mathbf{U}) = \mathbf{M}(\mathbf{r}) \text{vec}(\mathbf{U})$$

Where

$$\mathbf{M}(\mathbf{r}) = (\mathbf{N}^T(\mathbf{r}) \odot \mathbf{I})$$

The expression $\text{vec}(\hat{u}(\mathbf{r}) = \mathbf{N}^T(\mathbf{r}) \odot \mathbf{I} \text{vec}(\mathbf{U}))$ demonstrates how the field variable $\hat{u}(\mathbf{r})$ at the local coordinates \mathbf{r} can be represented and computed using shape functions $\mathbf{N}(\mathbf{r})$, the identity matrix, \mathbf{I} and the nodal values \mathbf{U} .

$$r_i = - \int \underline{\sigma}(d_i) : [\mathbf{B}]_i dV + \int_{S_T} \underline{T} \cdot \langle \mathbf{N}_i \rangle dS = 0 \dots \dots (19)$$

The above expression provides a compact representation of the equilibrium between internal and external forces.

$$\text{vec}(r_i) = - \int \mathbf{G}^T(\mathbf{r}) \text{vec}(\underline{\sigma}) dV + \int \mathbf{M}^T(\mathbf{r}) \cdot \text{vec}(\underline{T}) dS \text{ (from residual equation)}$$

$$\text{Mat}\left(\frac{\partial r_i}{\partial d_j}\right) = - \text{Mat}\left[\int [\mathbf{B}]_j : \frac{\partial \underline{\sigma}}{\partial \underline{\epsilon}} : [\mathbf{B}]_i dV\right]$$

$$= - \int \mathbf{G}^T(\mathbf{r}) \text{Mat}\left(\frac{\partial \underline{\sigma}}{\partial \underline{\epsilon}}\right) \mathbf{G}(\mathbf{r}) dV, \dots \dots (20) \text{ where } \text{Mat}([\mathbf{B}]) = \mathbf{G}(\mathbf{r})$$

i, j are skipped since i, j indicate i and j^{th} DOF. However, $\text{vec}(r_i)$ and $\text{Mat}\left(\frac{\partial r_i}{\partial d_j}\right)$ give non-zero values only within same element. $\text{vec}(r_i)$ and $\text{Mat}\left(\frac{\partial r_i}{\partial d_j}\right)$ are summed over all the elements, therefore, leaving out i and j .

$$dV = \det(\mathbf{J}(\mathbf{r})) dV_r$$

This relationship ensures the precise mapping of integrals over the element volume between global and local coordinate systems.

$$\text{vec}(r_i) = - \int \mathbf{G}^T(\mathbf{r}) \text{vec}(\underline{\sigma}) \det(\mathbf{J}(\mathbf{r})) dV_r + \int \mathbf{M}^T(\mathbf{r}) \cdot \text{vec}(\underline{T}) |\det \mathbf{J}^{-1}| dS_r$$

$$\text{Mat}\left(\frac{\partial r_i}{\partial d_j}\right) = - \int \mathbf{G}^T(\mathbf{r}) \text{Mat}\left(\frac{\partial \underline{\sigma}}{\partial \underline{\epsilon}}\right) \mathbf{G}(\mathbf{r}) \det(\mathbf{J}(\mathbf{r})) dV_r \dots \dots (21)$$

$\frac{\partial \underline{\sigma}}{\partial \underline{\epsilon}}$ is called the consistent tangent matrix and $\frac{\partial \underline{\sigma}}{\partial \underline{\epsilon}}$ must be calculated in the material routine.

➤ *FEM Coding & Solving Procedure:*

Displacement boundary condition,

$$\begin{aligned} \text{vec}(r_i) &= - \int \mathbf{G}^T(\mathbf{r}) \text{vec}(\underline{\sigma}) \det(\mathbf{J}(\mathbf{r})) dV_r + \int \mathbf{M}^T(\mathbf{r}) \cdot \text{vec}(\underline{T}) |\det \mathbf{J}^{-1}| dS_r \\ &= - \left[\int \mathbf{G}^T(\mathbf{r}) \text{Mat}\left(\frac{\partial \underline{\sigma}}{\partial \underline{\epsilon}}\right) \mathbf{G}(\mathbf{r}) \det(\mathbf{J}(\mathbf{r})) dV_r \right] \{d\} + \int \mathbf{M}^T(\mathbf{r}) \cdot \text{vec}(\underline{T}) |\det \mathbf{J}^{-1}| dS_r \dots \dots \dots (22) \end{aligned}$$

$$\text{vec}(r_i) = - [\mathbf{K}] \{d\} + \{R\} \dots \dots \dots (23)$$

where, $\text{Mat} \left(\frac{\partial r_i}{\partial \underline{\epsilon}} \right) \equiv \left[\int G^T(r) \text{Mat} \left(\frac{\partial \sigma}{\partial \underline{\epsilon}} \right) G(r) \det(J(r)) dV_r \right] \equiv [K]$; $\int M^T(r) \text{vec}(\underline{T}) \left| \det J J^{-1} \right| dS_r \equiv R$

The global DOF vector $\{d\}$ is partitioned into free (unknown) and prescribed (known) components based on displacement boundary conditions. $\{d\} = \begin{Bmatrix} d^f \\ d^p \end{Bmatrix}$

Where $\{d^f\}$ is the column vector regrouping all free DOFs and $\{d^p\}$ is the column vector regrouping all prescribed free DOFs. The residual equations are written as,

$$\begin{Bmatrix} \text{vec}(r_i)^f \\ \text{vec}(r_i)^p \end{Bmatrix} = - \begin{bmatrix} k^{ff} & k^{fp} \\ k^{pf} & k^{pp} \end{bmatrix} \begin{Bmatrix} d^f \\ d^p \end{Bmatrix} + \begin{Bmatrix} R^f \\ R^p \end{Bmatrix}$$

Note that d^p : i.e. prescribed displacement conditions, are already known.

$$\text{vec}(r_i)^f = - [k^{ff}] \{d^f\} - [k^{fp}] \{d^p\} + \{R^f\} \dots\dots\dots (24)$$

Therefore, instead of solving $\text{vec}(r_i) = - [K] \{d\} + \{R\}$, equation (24) is solved for $\{d^f\}$ following the Newton-Raphson procedure.

Note d^p , i.e. prescribed displacement conditions, are already known.

$$\text{vec}(r_i)^f = - [k^{ff}] \{d^f\} - [k^{fp}] \{d^p\} + \{R^f\} \dots\dots\dots (25)$$

Therefore, instead of solving $\text{vec}(r_i) = - [K] \{d\} + \{R\}$, equation (25) is solved for $\{d^f\}$ following the Newton-Raphson procedure.

➤ *MATLAB code function structure:*

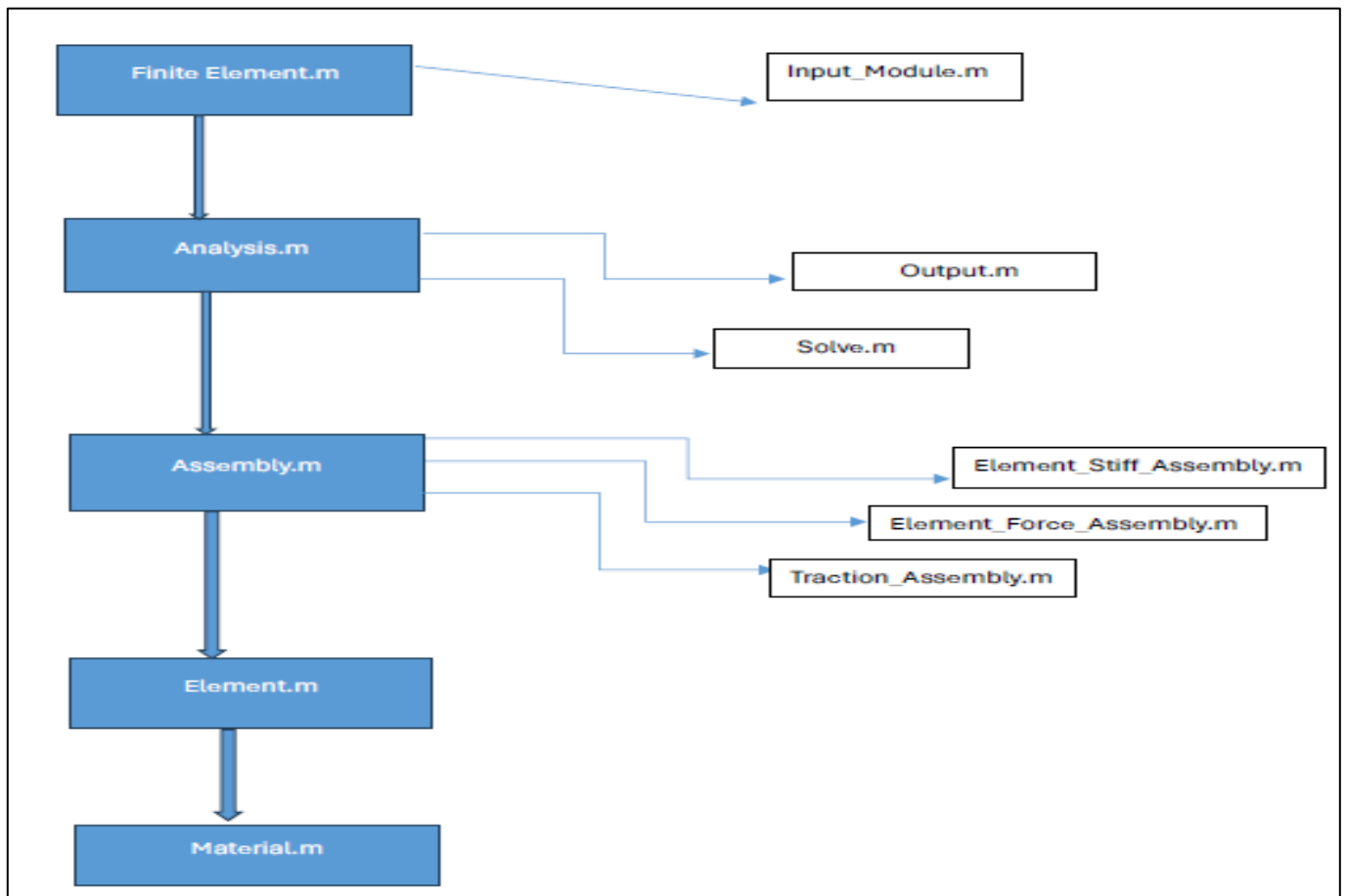


Fig 7 MATLAB Function Structure

- *MATLAB Function in Brief*

- ✓ **finite_element.m**: This is the main file that starts the code and calls input module.m to import the information of the B.V.P
- ✓ **input_module.m**: Imports the necessary information on the B.V.P., such as the numbers of nodes, elements, B.C., the connectivity of elements and materials information, etc.
- ✓ **analysis.m**: Performs the Newton-Raphson loop.
- ✓ **assembly.m**: Assembles $[K]$ and $[R]$ sums up $\sum[K]$, $\sum[R]$ from all elements.
- ✓ **ele_stiff_assembly.m**: Decomposes $[K]$ into $[k^{ff}]$, $[k^{fp}]$, $[k^{pf}]$, and $[k^{pp}]$
- ✓ **element_force_assembly.m**: Decomposes $[K] \{d\}$ into $- [[k^{ff}] [d^f] + [k^{fp}] [d^p]]$ and $- [[k^{pf}] [d^f] + [k^{pp}] [d^p]]$.
- ✓ **traction_assembly.m**: Decomposes $\{R\}$ into $[R^f]$ and $[R^p]$
- ✓ **element.m**: Calculates $[K]$ and $[K] \{d\}$ in each element.
- ✓ **material.m**: Calculates $\tilde{\sigma}$ and $\frac{\partial \tilde{\sigma}}{\partial \tilde{\epsilon}}$ in each Gauss point.

- *Verification of Matlab Code*

- *Verification Using One Element Model*

A three-dimensional CAD model with unit dimensions is created and meshed using a mesh size of 1. The analysis involves applying displacement boundary conditions to fix the bottom part of the element in the z-direction. The upper surface is given a displacement of 1. A plot is generated in Abaqus to show the relationship between the reaction force and displacement at the surface where the load is applied.

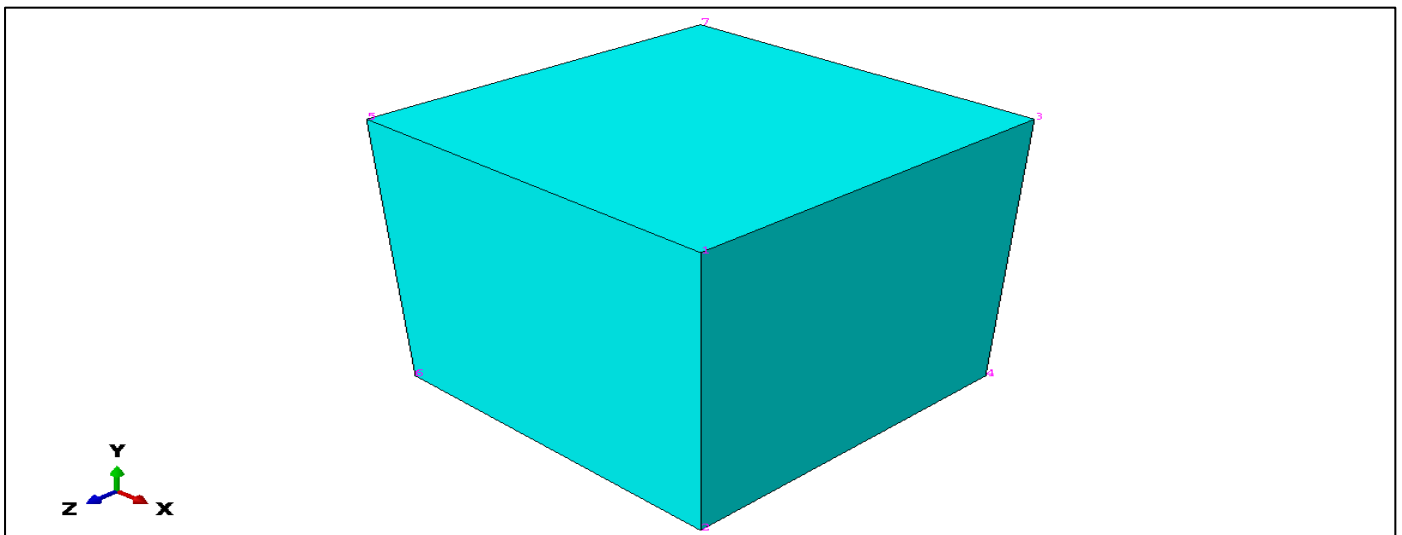


Fig 1 One Element Model

After the completion of the simulation, the INP file generated from Abaqus is used as an input file for the developed MATLAB code to plot a graph of reaction force against displacement. Since reaction force is plotted against the same node as that in the Abaqus simulation, the verification of the results is performed by plotting the results in the same graph as shown in Figure 9.

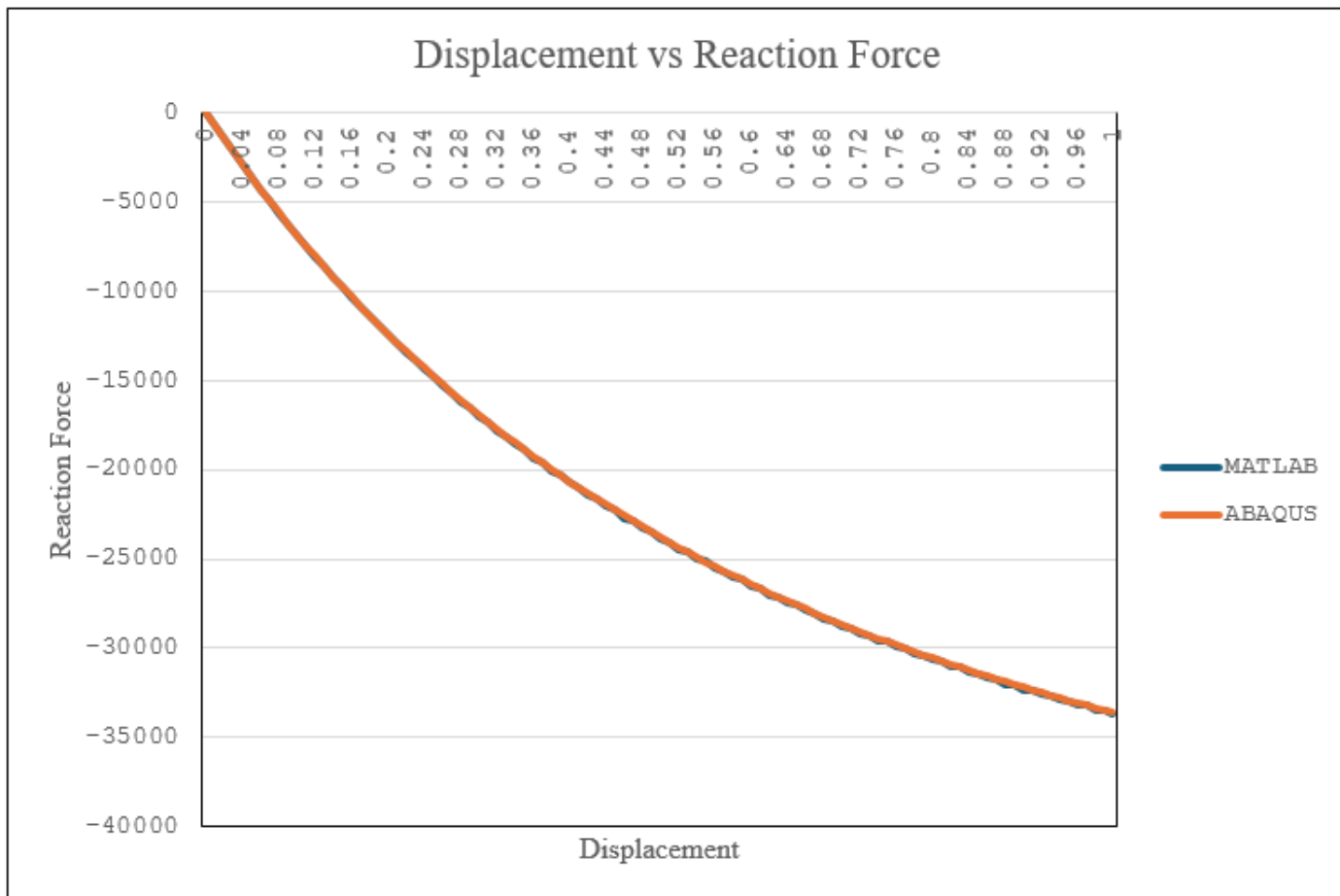


Fig 2 Reaction force vs displacement comparison for one element

In Figure 9, the blue line represents data derived from the MATLAB code, while the orange line signifies the data generated using Abaqus. The difference in Final Reaction force value between ABAQUS and MATLAB is 0.329%. The visual inspection of the figure also reveals a precise alignment between both data, indicating that the results from the MATLAB code align seamlessly with the Abaqus analysis.

➤ *Verification Using 8 Element Model*

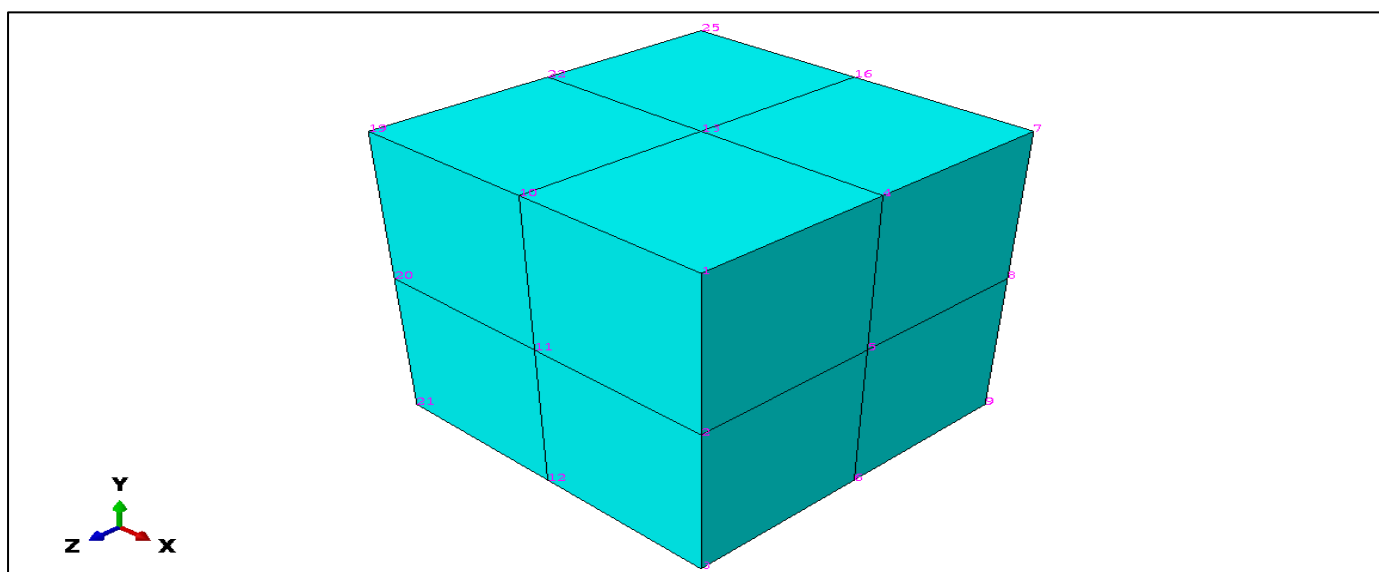


Figure 3 Meshing of 8-elements cube model

The model is meshed with a 0.5 mesh size to perform analysis with displacement boundary conditions in the z-direction with 8 elements, as shown in Figure 10. A plot of reaction force against displacement on the surface of load application is generated using Abaqus followed by MATLAB analysis.

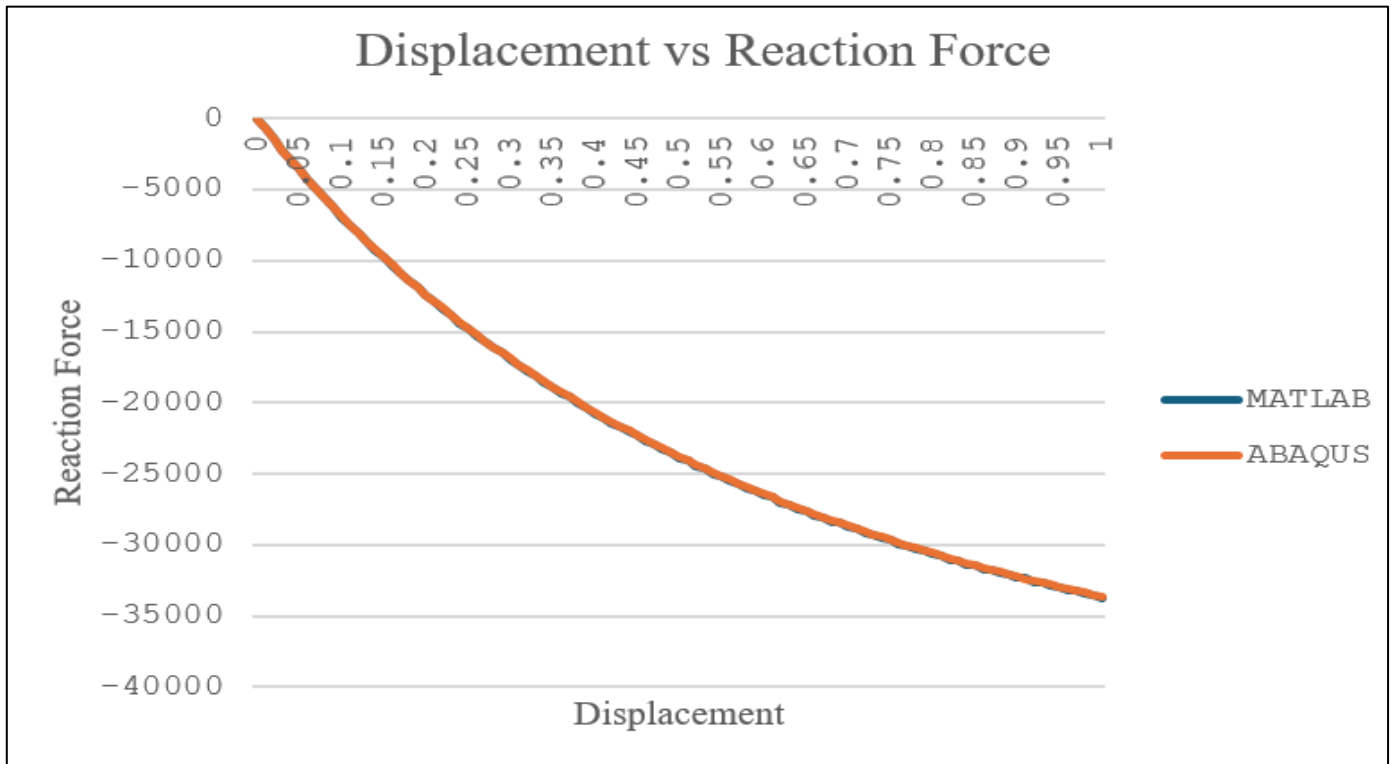


Fig 4 Reaction Force vs Displacement Comparison for 8-Element Model

➤ *Verification Using 64 Element Model*

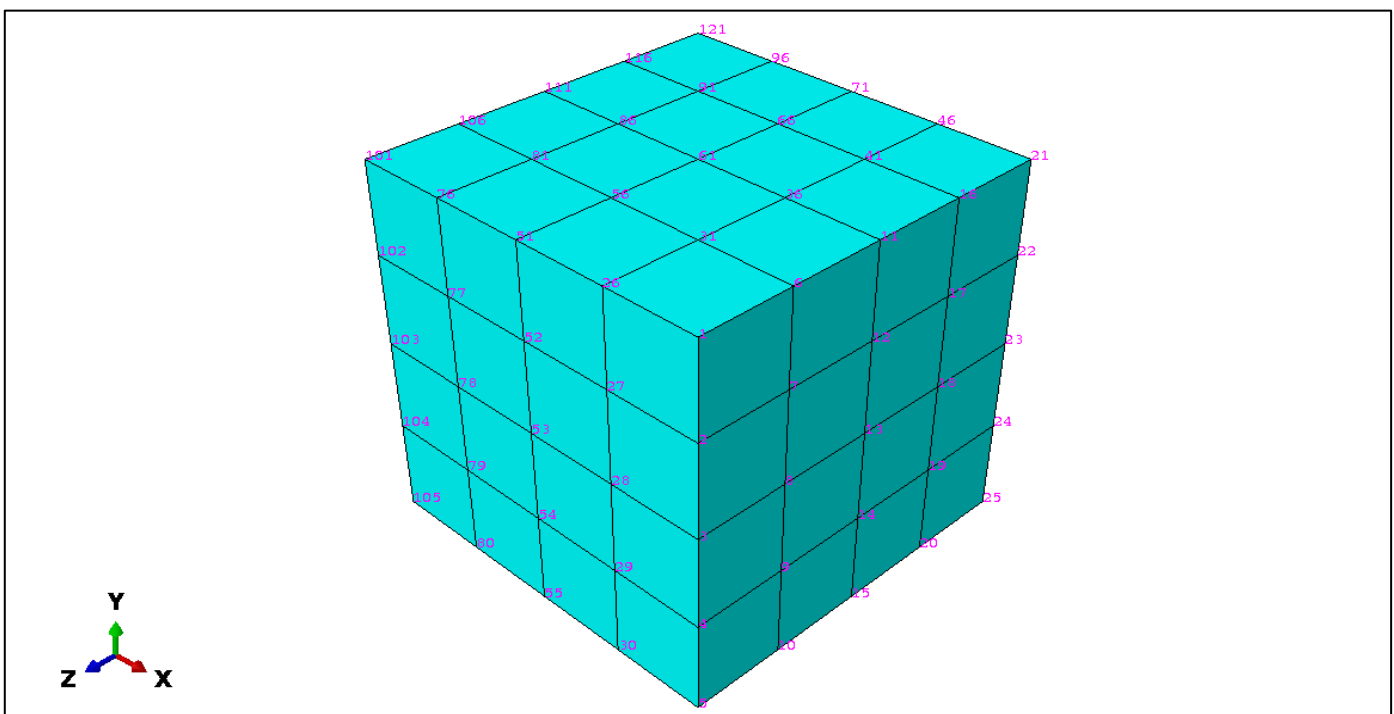


Fig 12 Meshing of 64-Elements Cube Model

A model is composed of 64 elements, as shown in Figure 12, with displacement boundary conditions such as those for the 8-element model. Analysis is performed on Abaqus followed by MATLAB analysis. Figure 13 shows reaction force versus

displacement obtained through both Abaqus and MATLAB analyses. Notably, this agreement is consistent for a 8 as well as single element model, further confirming the accuracy and reliability of the MATLAB code results in comparison to Abaqus.

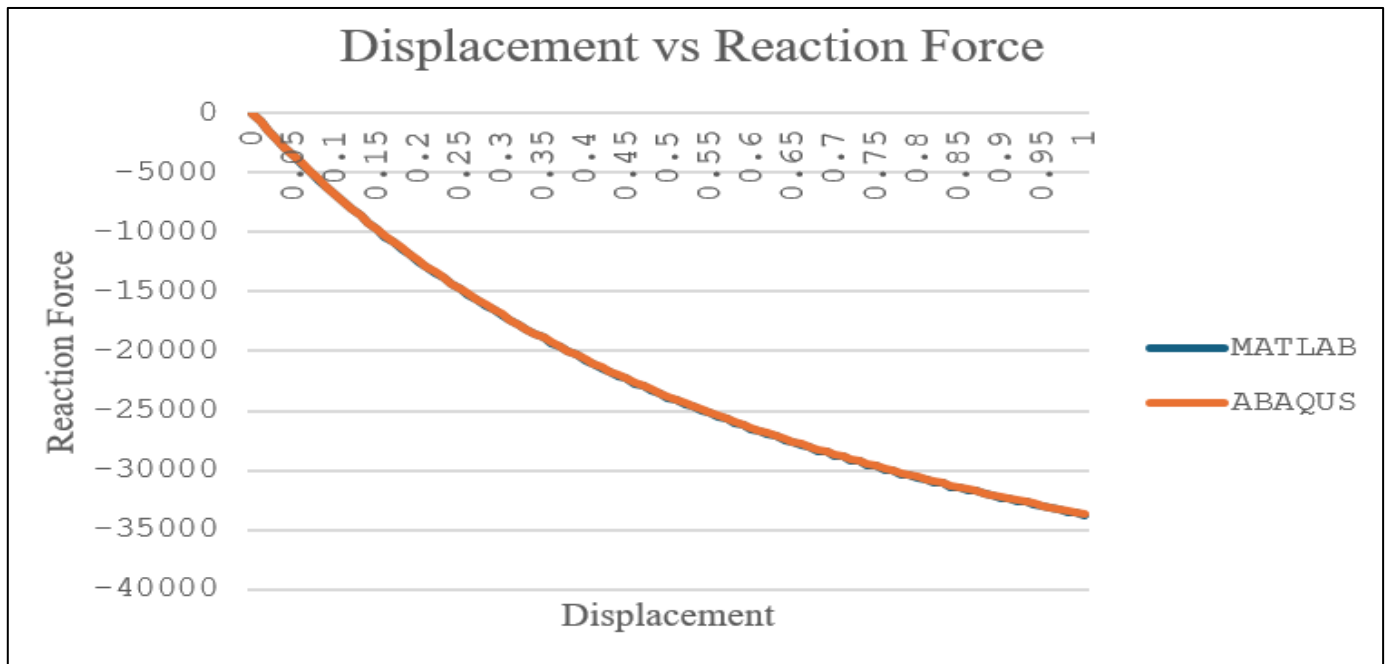


Fig 5 Reaction Force vs Displacement Comparison For 64-Element Model

CHAPTER FOUR MODELING AND SIMULATION

➤ *Theoretical Background*

The area moment of inertia (AMI) is a fundamental property in structural and mechanical engineering that helps to determine an object's resistance to bending and torsion. It is particularly useful when analyzed along different axes because the structural response of a component depends on the loading direction and cross-sectional geometry.

The area moment of inertia is given by the following formula:

$$I = I_c + A \cdot d^2 \dots\dots\dots (26)$$

Where I_c is the centroidal moment of inertia of the individual section, A is the area of the section, and d is the perpendicular distance between the centroid of the section and the reference axis.

In this analysis, the overall cross section is subdivided into three distinct rectangular components, labeled I_1 , I_2 and I_3 . The total moment of inertia is then obtained by computing the moment of inertia for each rectangle with respect to the reference axis

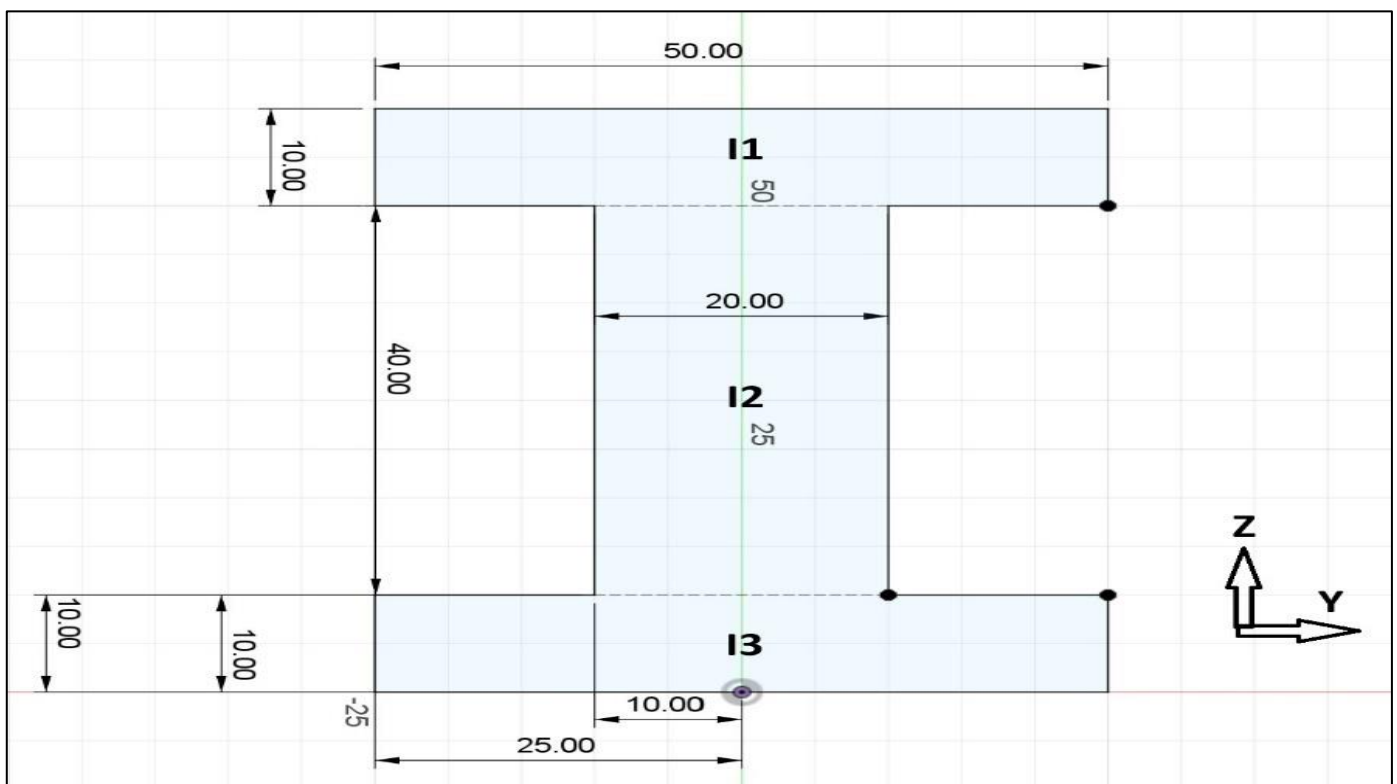


Fig 6 Cross Section of Front Axle

➤ *Moment of Inertia about Z-Axis (I_z):*

$$I_z = I_1 + I_2 + I_3$$

$$= \frac{1}{12} * 10 * 50^3 + 10 * 50 * 0^2 + \frac{1}{12} * 40 * 20^3 + 40 * 20 * 0^2 + \frac{1}{12} * 10 * 50^3 + 10 * 50 * 0^2$$

$$I_z = 2.35 * 10^{-7} \text{ m}^4$$

➤ *Moment of Inertia about Y-Axis (I_y):*

$$I_y = I_1 + I_2 + I_3$$

$$= \frac{1}{12} * 50 * 10^3 + 10 * 50 * 25^2 + \frac{1}{12} * 20 * 40^3 + 20 * 40 * 0^2 + \frac{1}{12} * 50 * 10^3 + 10 * 50 * 25^2$$

$$I_y = 7.4 * 10^{-7} \text{ m}^4$$

The detailed moment of inertia calculations is crucial for ensuring the axle’s strength and stability in automotive applications. The results indicate that the Y-axis moment of inertia (I_y) is approximately double the Z-axis moment of inertia (I_z), which suggests that the front axle is primarily designed to handle vertical loads rather than crash impact forces. This makes sense because the primary function of the axle is to support the vehicle's weight and transfer loads efficiently, rather than absorb high-impact crash forces.

➤ *Design*

FEA (Finite Element Analysis) on the structure of a front axle is carried out analyzing stress distribution developed by the application of a crash load at a specified boundary. Different types of analyses can be done on the axle such as static analysis, modal, harmonic, transient dynamic and buckling analysis. The present research uses Abaqus to perform static analysis on the axle.

Since the front axle is symmetrical, it is divided into two sections, and only the right section is considered for analysis.

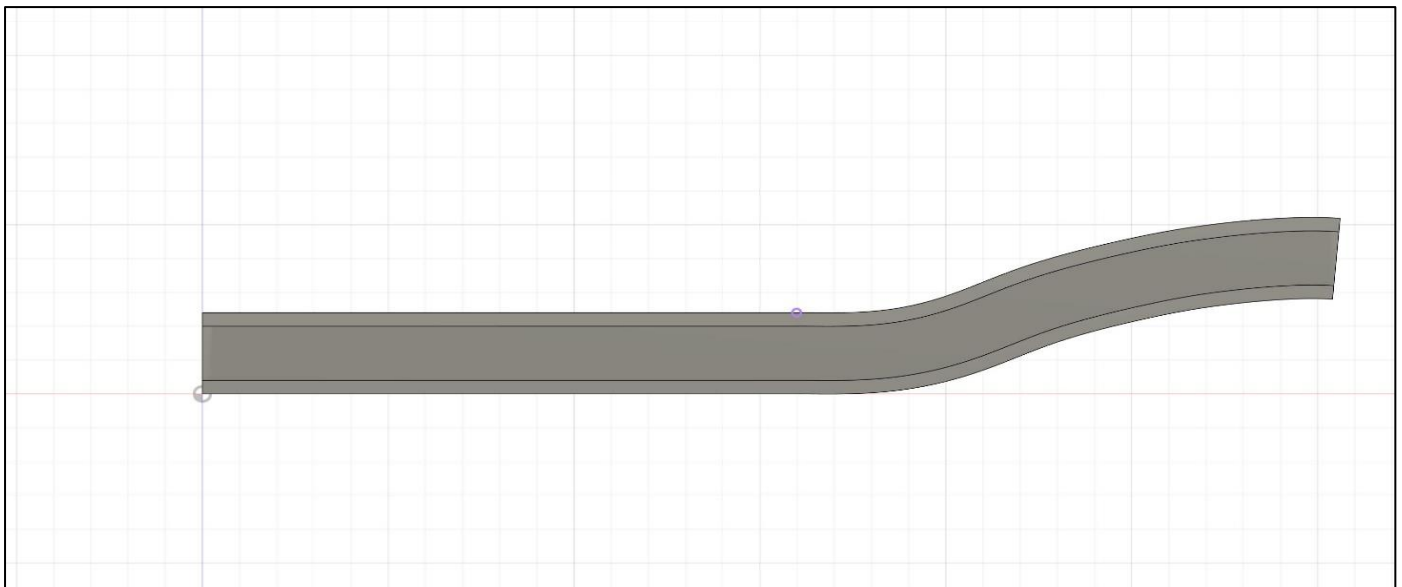


Fig 15 Left View of Front Axle

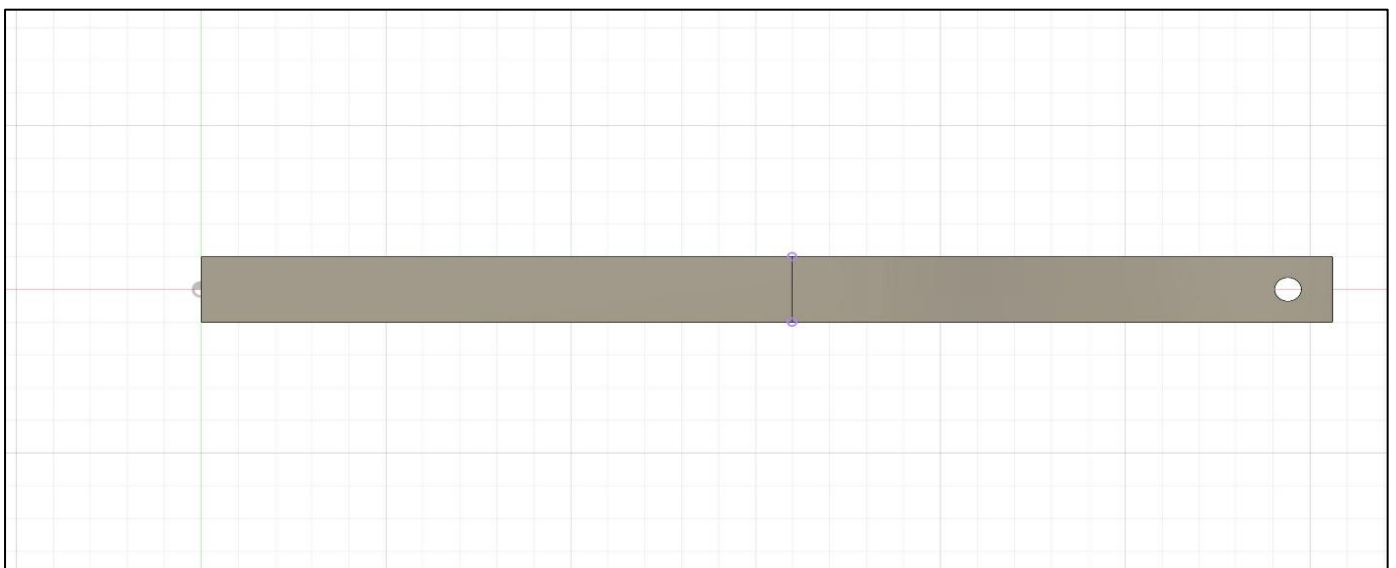


Fig 16 Top View of Front Axle

Firstly, the front axle’s Computer Aided Design (CAD) model is completed as shown in Figures 2 and 3. For analysis purposes, a simple design of the front axle is considered. The reason behind considering only a simple design is to reduce the complexity of the model and to save computational time in Abaqus.

➤ *Model Definition*

Two optimized models are designed by varying the dimensions of the center body and kingpin diameter.

Table 1 Model Definition

		Material	a (mm)	Kingpin diameter (mm)
Existing Design	Model 1	AISI 4140	20	18
Optimized Design	Model 2	AISI 4140	30	25

A simple front axle is modeled using Fusion 360, as illustrated in Figures 1 and 2. The measurements were taken from a 2007 Toyota Tacoma Truck. The total length of the front axle is 1520 mm, resulting in a half-section length of 760 mm. The axle width measures 50 mm, while the body width is varied. The flange height is 10 mm, and the overall height of the front axle is 60 mm.

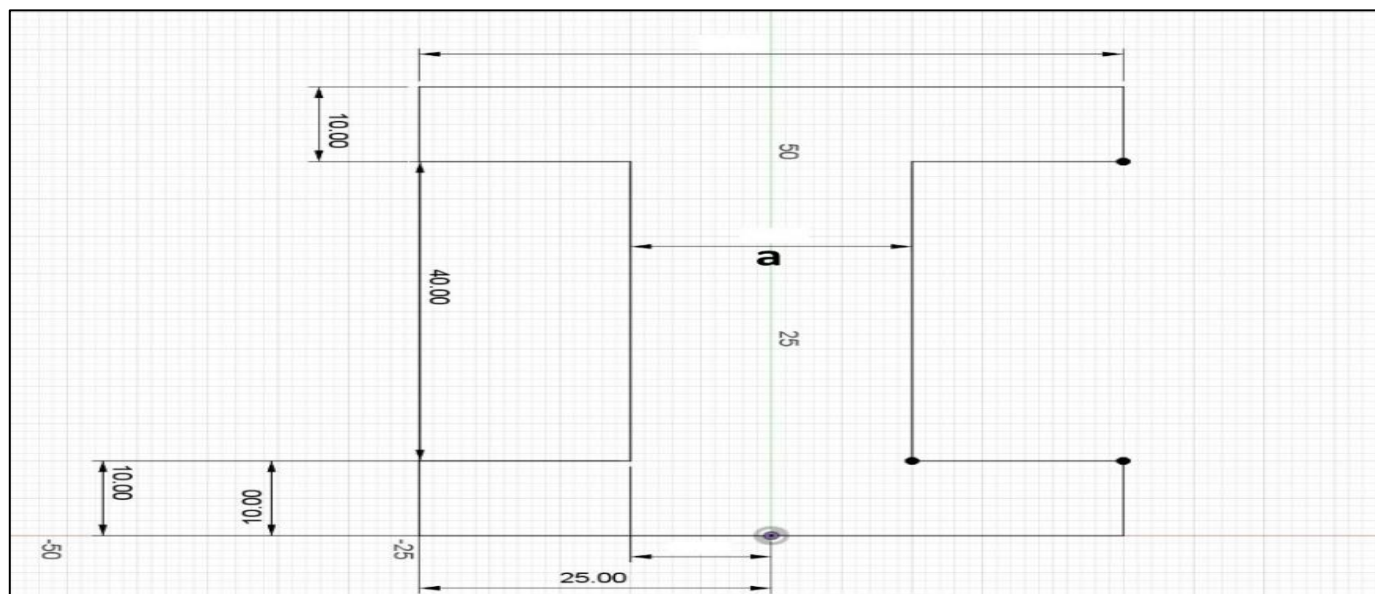


Fig 7 Model Parameters for Modifications

➤ *Static Analysis*

A simple front axle model is designed in Fusion 360 as shown in Figures 1, 2, and 3. The CAD model is then exported in STEP file and imported in ABAQUS for computation. The model's simplicity is considered for the analysis to save computational time. AISI 4140 Stainless steel is used for the study. The mechanical property of the material is shown in Table 1 and the material composition of that material is shown in Table 2.

Table 2 Mechanical Properties of Material

Parameters	4140 Stainless Steel
Ultimate Strength	655 MPa
Poisson's Ratio	0.30
Yield Strength	415 MPa
Modulus of Elasticity	210 GPa
Shear Modulus	80 GPa

Table 3 Material Composition

Material Composition	4140 Stainless Steel
Iron	≥ 50%
Chromium, Cr	0.80 - 1.10
Manganese, Mn	0.75 - 1.0
Carbon, C	0.380 - 0.430
Silicon, Si	0.15 - 0.30
Molybdenum, Mo	0.15 - 0.25
Sulfur, S	0.040
Phosphorous, P	0.035
Chromium, Cr	0.80 - 1.10

➤ *Boundary Conditions*

The boundary conditions are illustrated in Figure 5, denoted as (A) and (B). These conditions impose constraints on the X, and Z axes at the edge surface, with prescribed displacements set to $U_1 = 0$ and $U_3 = 0$ as shown in Figure 5 (A). The center of the axle can move in the y-direction. In Figure 5 (B), constraints on the X, Y and Z axes are imposed at the kingpin surface, with prescribed displacements set to $U_1 = 0, U_2 = 0$ and $U_3 = 0$.

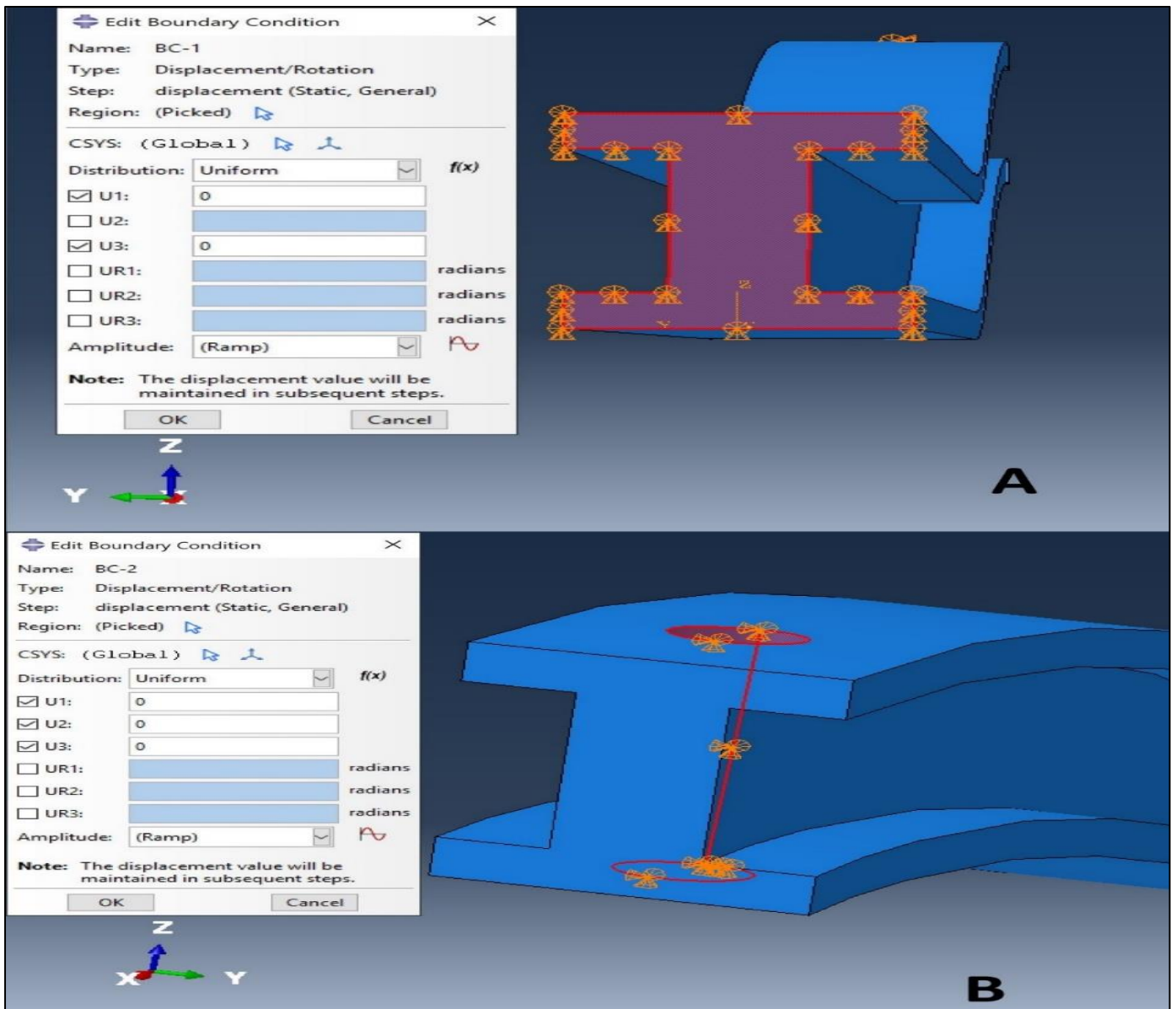


Fig 8 Boundary Conditions at the Center (A) and Kingpin (B)

➤ *Loading Conditions*

During the analysis, crash load conditions are applied to check maximum stress due to a front collision of a car. The calculation is given below:

Total weight of a car = 1000 kg

Impact Speed(v) = 35 mph = 15.6 m/s

Here the impact time is assumed as, $\Delta t = 0.3s$

Acceleration(a) = $v/t = 15.6/0.3 = 52 \text{ m/s}^2 = 5.3g$

Crash Load (L_c) = $m \cdot a = 52 \text{ KN}$

Since only half of the front axle is being analyzed, the crash load is taken to be 26 kN. The front axle is connected to the chassis through spring plates, which transfer the crash load to the front axle in the event of a frontal collision. The contact area between the spring plates and the front axle is 100 mm × 50 mm, resulting in a total contact area of 5000 mm².

The surface traction acting on this contact area can be determined using the formula:

$$T = L_c / A_c$$

Where

L_c is the crash load (26 kN) and A_c is the contact area (5000 mm²). Substituting these values yields:

$$T = 5.2 \text{ MPa}$$

This surface traction will be applied to the contact area in the y-direction during the finite element analysis (FEA) of the front axle to evaluate its structural response under crash conditions.

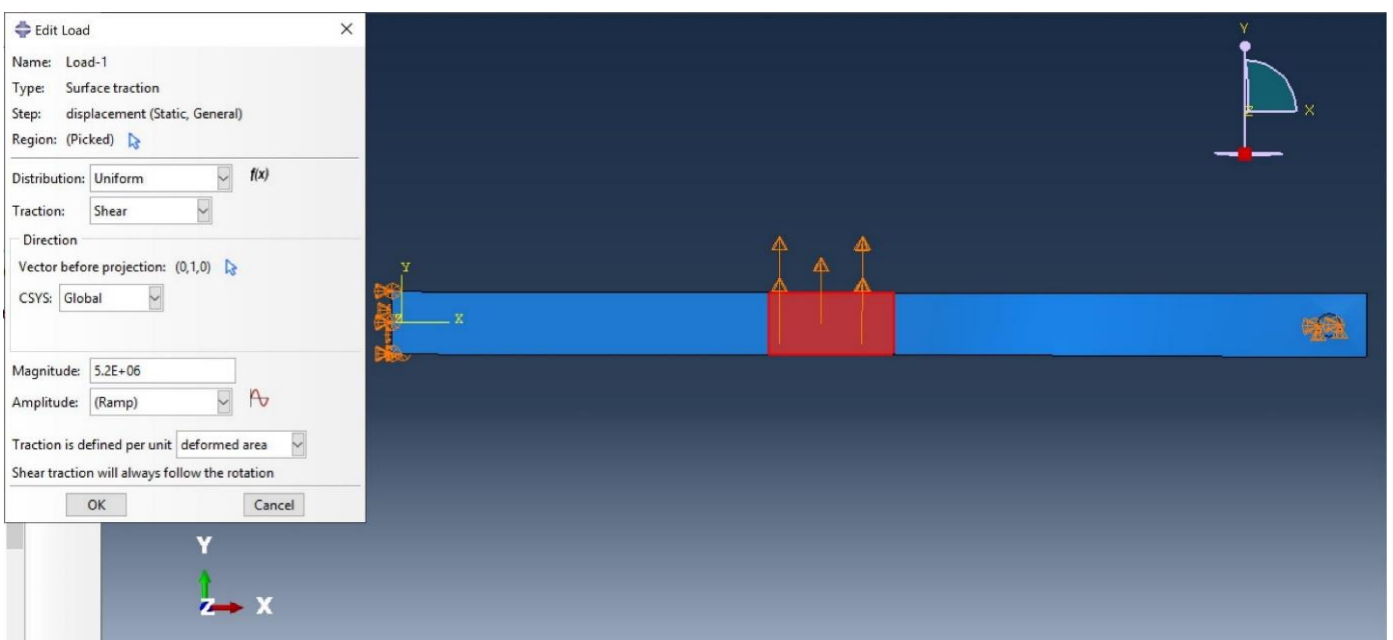


Fig 9 Loading Conditions at the Contact Area

➤ *Mesh*

For this analysis, a tetrahedral mesh is used as shown in Figure 7. The reason behind choosing a tetrahedral mesh with C3D10 quadratic element type is due to its ability to provide more accurate results in complex geometries. Different mesh sizes are used in the models to check convergence.

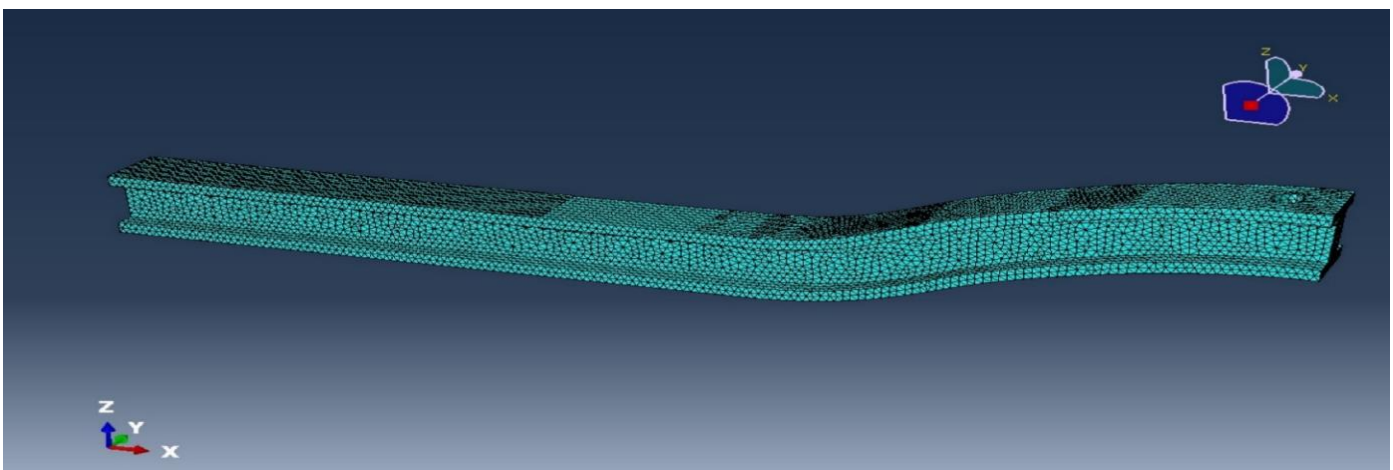


Fig 10 Tetrahedral Mesh on Model

CHAPTER FIVE RESULT AND ANALYSIS

Once all the models are meshed followed by defining boundary conditions as well as loading conditions, a job is created to analyze stress in the model. The maximum equivalent stress encountered on the front axle is noted to understand the stability of the model in terms of the factor of safety during a frontal crash. All the models are analyzed for different element sizes. Boundary conditions are the same for all the mesh sizes.

To evaluate the structural performance of the front axle, both elastic and elasto-plastic analyses are conducted. The elastic analysis is performed to assess the initial stress under crash loads, while the elasto-plastic analysis provides insights into the deformation behavior beyond the yield point, ensuring the design can withstand extreme loading conditions such as crash impacts. Since the model is loaded with an approximately 5G load, a factor of safety greater than 1 is considered to be sufficient to draw a conclusion whether the design is safe to operate or not.

➤ *Model 1*

- *Elastic Analysis*

Model 1 was subjected to elastic analysis using three different mesh sizes to investigate stress distribution under loading. The results indicate that convergence in stress values occurs around a mesh size of 5 mm. The maximum von Mises stress observed in this case is approximately 1184 MPa. It is important to note that the factor of safety cannot be evaluated for elastic analysis alone, as this analysis does not account for yielding or permanent deformation.

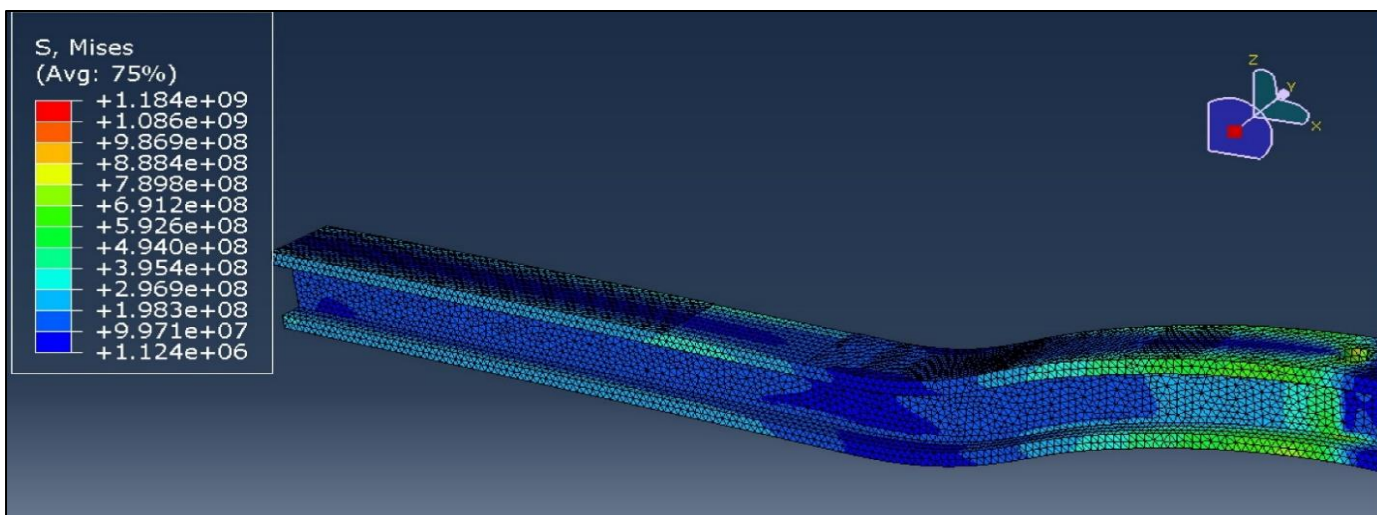


Fig 11 Model 1: Elastic Analysis

➤ *Elastoplastic Analysis*

Elastoplastic analysis is also performed on Model 1 across three mesh sizes. Similar to the elastic case, stress convergence is observed around a mesh size of 5 mm. The maximum von Mises stress recorded in this elastoplastic analysis was 519.8 MPa. Since the input of yield strength versus plastic strain includes hardening, i.e., the increase of yield strength with respect to plastic strain, the yield strength keeps increasing as strain increases (i.e., as deformation develops).

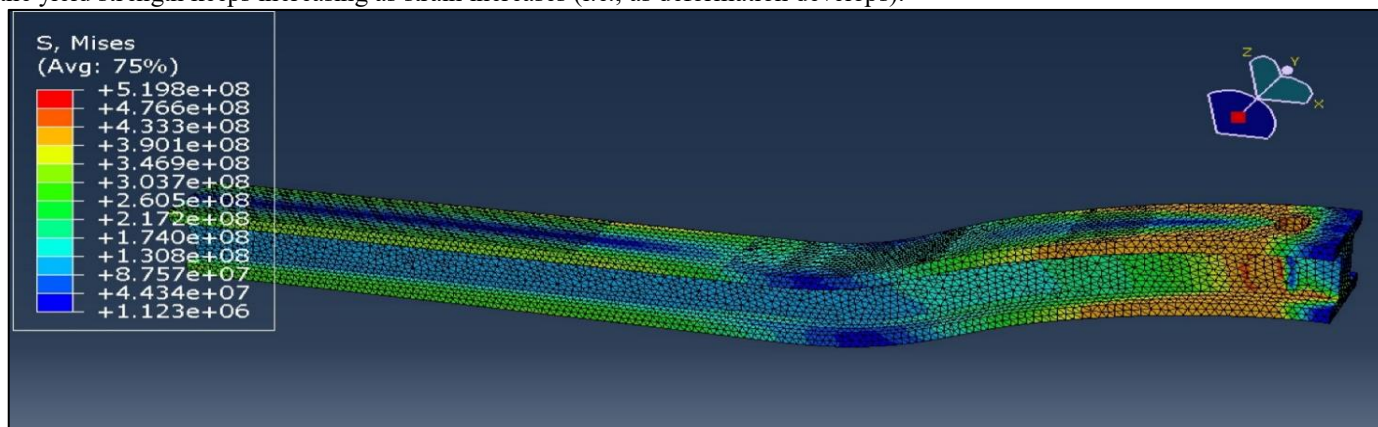


Fig 12 Model 1: Elastoplastic Analysis

➤ *Model 2*

• *Elastic Analysis*

Model 2 is analyzed using elasticity only for three mesh sizes. Based on the stress distribution contour, the maximum stress is 706 MPa for a mesh size of 5 mm in the elastic case.

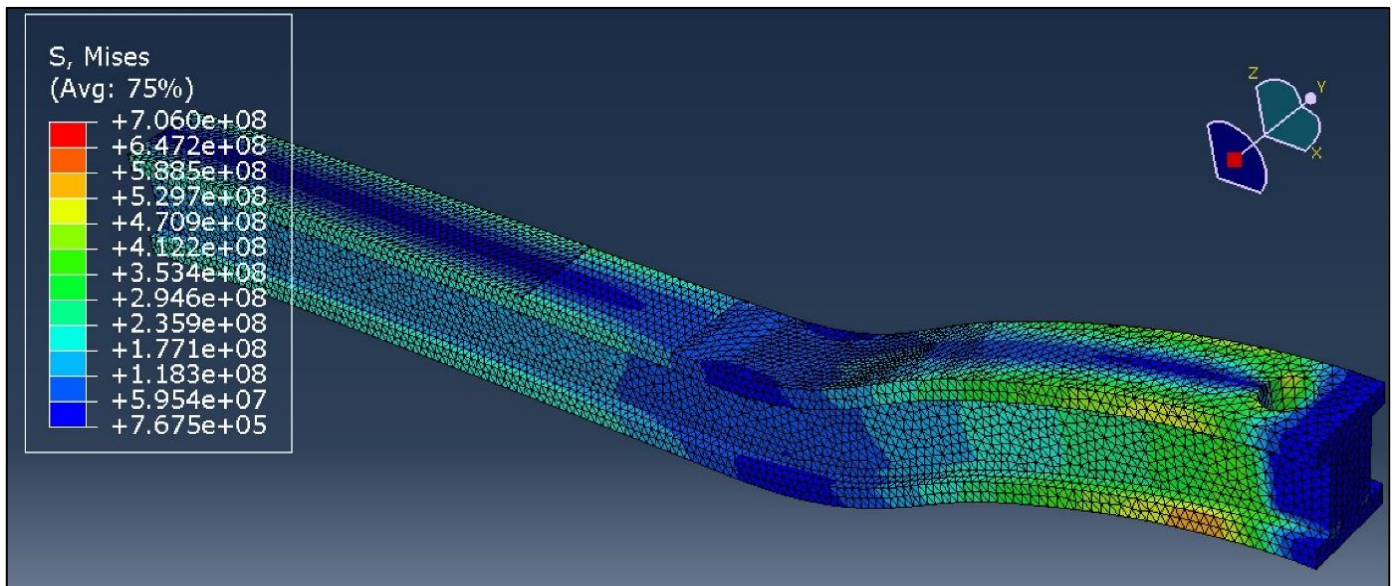


Fig 13 Model 2: Elastic Analysis

➤ *Elastoplastic Analysis*

Model 2 is analyzed using elastoplasticity for three mesh sizes. In this case too, convergence occurs around a mesh size of 5mm. Based on the stress distribution contour, the maximum stress is 415.5 MPa in the elastoplastic case.

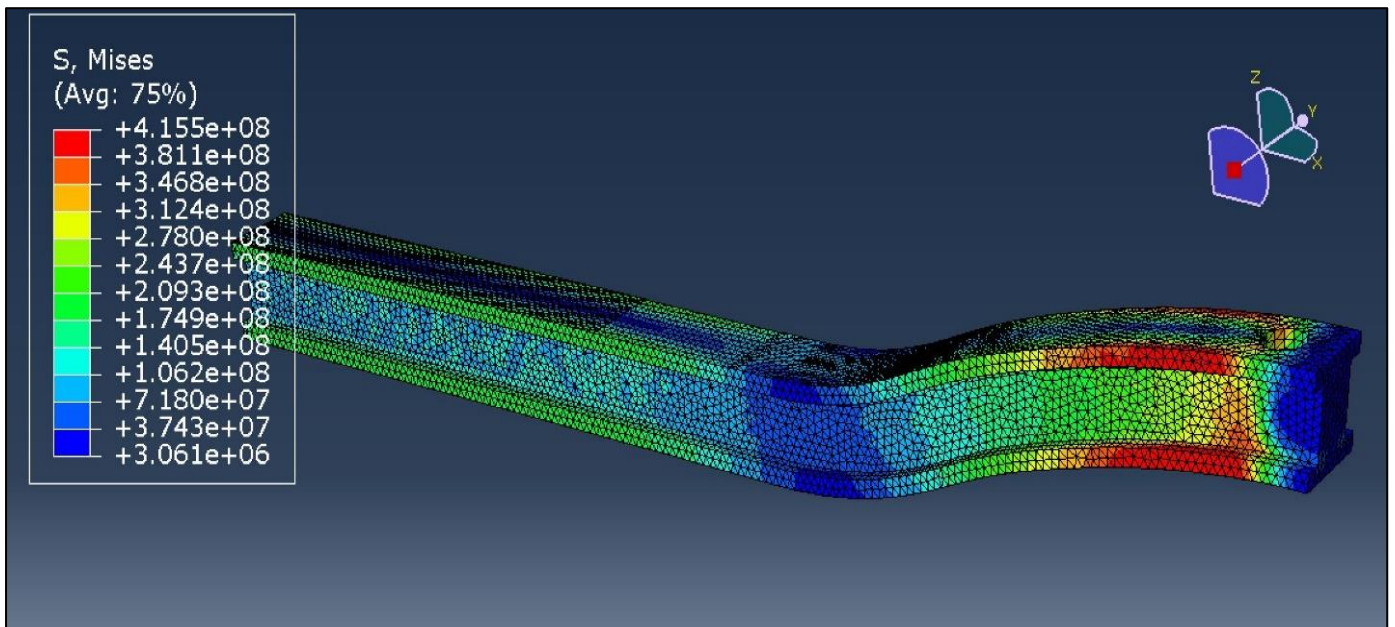


Fig 14 Model 2: Elastoplastic Analysis

➤ *Summary of the results*

Table 4 Summary of Simulation Results

Model 1: Existing Design							
Elastic Analysis				Plastic Analysis			
Mesh Size	Maximum Von Mises Stress (Mpa)	Yield Strength (Mpa)	Factor of Safety	Mesh Size	Von Mises Stress (Mpa)	Maximum Yield Strength (Mpa)	Factor of Safety
5	1184	415	0.35	5	519.8	415	0.80
6	1139	415	0.36	6	547.9	415	0.76
8	1193	415	0.35	8	576.9	415	0.72
Yield Strength	415MPA			Yield Strength	415MPA		
Poissons ratio	0.3			Poissons ratio	0.3		
Youngs Modulus	210 GPA			Youngs Modulus	210 GPA		
Model 2: Optimized Design							
Elastic Analysis				Plastic Analysis			
Mesh Size	Maximum Von Mises Stress (Mpa)	Yield Strength (Mpa)	Factor of Safety	Mesh Size	Maximum Von Mises Stress (Mpa)	Yield Strength (Mpa)	Factor of Safety
5	706	415	0.59	5	415.5	415	1.00
6	662.1	415	0.63	6	435.6	415	0.95
8	638.6	415	0.65	8	486.5	415	0.85
Yield Strength	415MPA			Yield Strength	415MPA		
Poissons ratio	0.3			Poissons ratio	0.3		
Youngs Modulus	210 GPA			Youngs Modulus	210 GPA		

It is observed from the results shown in Table 3 that the optimized model experiences a lower maximum stress leading to an increase in factor of safety. With a factor of safety 1, it is affirmed that the optimized design is sufficiently safe to withstand the frontal crash load of 5G.

CHAPTER SIX

CONCLUSION

In this study, Finite Element Analysis (FEA) is conducted on the front axle of a car using Abaqus to evaluate the structural integrity of the design under a crash load applied in the Y-direction. The methodology presented can be effectively utilized to optimize the geometry and thickness of the front axle. By systematically varying design parameters, configurations that meet desired safety criteria with an adequate factor of safety can be identified. This approach demonstrates how advanced simulation tools can be employed to address real-world engineering challenges and support informed design decisions.

REFERENCES

- [1]. Min Zhang, Xiangfei Ji, Lijun Li, “A research on fatigue life of front axle beam for heavy duty truck”, *Advances in Engineering Software* 91(2016): 63-68
- [2]. Shwetank Avikal, Atul Bisht, Devender Sharma, Himanshu Hindwan, Siddharth Yadav, K.C. Nithin Kumar, Padmanabh Thakur, “Design and fatigue analysis of front axle beam of a heavy duty truck using ANSYS”, *Materials Today: Proceedings* 26(2020) 3211-3215
- [3]. M.M. Topac , H. Gunal , N.S. Kuralay, “Fatigue failure prediction of a rear axle housing prototype by using finite element analysis” , *Engineering Failure Analysis* 16 (2009) 1474–1482
- [4]. Hemant L. Aghav, M.V.Walame, “ Stress Analysis and Fatigue Analysis of Front Axle of Heavy-Duty Truck using ANSYS Ncode Design Life for Different Loading Cases”, *Int. Journal of Engineering Research and Application* ISSN : 2248-9622, Vol. 6, Issue 6, (Part -2) June 2016, pp.78-82
- [5]. Zheng B, Fu S, Lei J, “Topology Optimization and Multiobjective Optimization for Drive Axle Housing of a Rear Axle Drive Truck.” *Materials (Basel)*. 2022 Jul 30;15(15):5268. doi: 10.3390/ma15155268. PMID: 35955204; PMCID: PMC9369993.
- [6]. Pratyush Deshmukh, Lohit Kumar, Dixit Kumar Maradia and Gunchita Kaur Wadhwa “TOPOLOGY OPTIMIZATION OF REAR AXLE OF HEAVY VEHICLE.” *International Journal of Mechanical Engineering and Technology (IJMET)* Volume 9, Issue 4, April 2018, pp. 953 959
- [7]. Nikita A Duple, A. D. Diwate “Design and Finite Element Analysis of Differential Cover for Rear Drive axle of a Light Commercial Vehicle (LCV).” *International Journal of Analytical, Experimental and Finite Element Analysis* Vol. 7, Issue. 2, July 2020, pp 53 – 60.
- [8]. Sainadh, A. A. (2018). DESIGN, ANALYSIS & OPTIMIZATION OF FRONT AXLE IN ELECTRIC VEHICLES. *INTERNATIONAL JOURNAL OF ENGINEERING SCIENCES & RESEARCH TECHNOLOGY*, 7(8), 557-567.
- [9]. N. León, O. Martínez, P. Orta C., P. Adaya, “Reducing the Weight of a Frontal Truck Axle Beam Using Experimental Test Procedures to Fine Tune FEA. *MSC Automotive Conference.*, 2000
- [10]. K.V. Dhande, P. Ulhe, “Design and analysis of front axle of a heavy commercial vehicle”, *E3S Int. J. Sci., Technol. Manage.* (2014), pp. 114-122
- [11]. M.M. Topic, S. Ercan, N.S. Kuralay “Fatigue life prediction of a heavy vehicle steel wheel under radial loads by using finite element analysis” *Eng. Fail. Anal.*, 20 (2012), pp. 67-79